Theory of two-dimensional Fourier transform electron spin resonance for ordered and viscous fluids

Sanghyuk Lee, David E. Budil, and Jack H. Freed
Baker Laboratory of Chemistry, Cornell University, Ithaca, New York 14853-1301

(Received 4 April 1994; accepted 15 June 1994)

A comprehensive theory for interpreting two-dimensional Fourier transform (2D-FT) electron spin resonance (ESR) experiments that is based on the stochastic Liouville equation is presented. It encompasses the full range of motional rates from fast through very slow motions, and it also provides for microscopic as well as macroscopic molecular ordering. In these respects it is as sophisticated in its treatment of molecular dynamics as the theory currently employed for analyzing cw ESR spectra. The general properties of the pulse propagator superoperator, which describes the microwave pulses in Liouville space, are analyzed in terms of the coherence transfer pathways appropriate for COSY (correlation spectroscopy), SECSY (spin–echo correlation spectroscopy), and 2D-ELDOR (electron–electron double resonance) sequences wherein either the free-induction decay (FID) or echo decay is sampled. Important distinctions are made among the sources of inhomogeneous broadening, which include (a) incomplete spectral averaging in the slow-motional regime, (b) unresolved superhyperfine structure and related sources, and (c) microscopic molecular ordering but macroscopic disorder (MOMD). The differing effects these sources of inhomogeneous broadening have on the two mirror image coherence pathways observed in the dual quadrature 2D experiments, as well as on the auto vs crosspeaks of 2D-ELDOR, is described. The theory is applied to simulate experiments of nitroxide spin labels in complex fluids such as membrane vesicles, where the MOMD model applies and these distinctions are particularly relevant, in order to extract dynamic and ordering parameters. The recovery of homogeneous linewidths from FID-based COSY experiments on complex fluids with significant inhomogeneous broadening is also described. The theory is applied to the ultraslow motional regime, and a simple method is developed to determine rotational rates from the broadening of the autopeaks of the 2D-ELDOR spectra as a function of the mixing time, which is due to the development of "motional crosspeaks." The application of this method to recent experiments with nitroxide probes illustrates that rotational correlation times as slow as milliseconds may be measured. It is shown how 2D-ELDOR can be useful to distinguish between the cases of very slow motional (SM) rates with little or no ordering and of very high ordering (HO) but substantial motional rates even though the cw ESR spectra are virtually the same. The effects of motion and of microscopic ordering on the nuclear modulation patterns in 2D-FT-ESR are compared, and it is suggested that these effects could be utilized to further distinguish between SM and HO cases. Key aspects of the challenging computational problems are discussed, and algorithms are described which lead to significant reductions in computation time as needed to permit nonlinear least-squares fitting of the theory to experiments.

I. INTRODUCTION

Recent developments in digital electronics and microwave technology have opened the new field of two-dimensional Fourier transform (2D-FT) electron spin resonance (ESR) where the full ESR spectrum is excited by the microwave pulses and the full free induction decay (FID) or echo decay is sampled. Gorcester and Freed applied COSY (correlation spectroscopy), SECSY (spin–echo correlation spectroscopy), and 2D-ELDOR (electron–electron double resonance) sequences to nitroxides in the fast motional regime, where the FID is detected, and were able to demonstrate the enhanced resolution to spin relaxation mechanisms.[1–3] Patyal *et al.* extended their applicability for determining rotational motional rates in the very slow motional regime and the (near) rigid limit, wherein the echo decay is detected.[4,5] Recently, as a result of even shorter (~50 ns) spectrometer deadtimes it has been possible to collect the full FID from spectra obtained in complex fluids such as membrane vesicles, despite the very short T_2^*'s of 20–30 ns.[6,7] These spectra are characterized by significant inhomogeneous broadening and motional rates in the incipient slow motional regime. These initial studies have demonstrated the great potential value of 2D-FT ESR in the study of complex fluids, and have indicated the importance of a rigorous quantitative theory for their analysis. The original analyses of Gorcester and Freed are appropriate mainly for the fast motional regime in the absence of significant inhomogeneous broadening.

Over the years, the quantitative analysis of slow-motional cw ESR spectra has mainly depended on computer simulations based on the stochastic Liouville equation (SLE).[8,9] The significant computational challenges in simulating cw ESR spectra have been successfully dealt with by the implementation of the Lanczos algorithm,[10,11] by the de-

velopment of a basis set minimization scheme,[12] and by nonlinear least-squares fitting of the simulations to experiment.[13,14] Extensions to more sophisticated models have also been made.[15,16]

Schwartz *et al.* developed a theoretical framework for time domain ESR for very slow rotational motion based on the SLE. It focused on spin–echo phenomena.[17–19] and it proved useful in initial experiments utilizing magnetic field-swept 2D-ESE (electron-spin-echo) methods[11,19,20] despite its approximate nature (e.g., restriction to axial tensors and isotropic fluids). This theory was used in an approximate fashion to provide a preliminary analysis of the experiments of Patyal *et al.*[4,5] With the advent of 2D-FT ESR and the ability to select a specific coherence transfer pathway of the density matrix in a multiple pulse sequence, the quantitative analysis of 2D spectra requires a more general and rigorous theory, which also encompasses the full range of motional rates, and which can include both microscopic and macroscopic molecular ordering. We have now developed such a theory of 2D-FT ESR that is applicable over the entire motional range. It is equivalent to the most sophisticated cw ESR theory in its description of the molecular dynamics but it is necessarily considerably more sophisticated with respect to the spin dynamics.

Rigorous simulation of a 2D-FT ESR spectrum by the SLE is a challenging problem both in its theoretical and computational aspects. In Sec. II we develop the general formulation which is based on the analysis of the coherence transfer pathways for COSY, SECSY, and 2D-ELDOR. Within this framework it is possible to partition the matrix representation of the SLE into subspaces distinguished by their coherence order, that are appropriate for the evolution periods when there is no microwave radiation. This greatly simplifies the analysis and the computational challenges. Fundamental symmetries are introduced to further reduce the size of the matrix representations of the SLE. The general properties of the pulse propagator superoperator, which describes the effects of the microwave pulses in Liouville space, are presented. The approach described is sufficiently general to be applied to an arbitrary pulse sequence.

Despite the simplifications achieved in Sec. II, the computational challenge for 2D-FT ESR is much greater than for cw ESR. This is due partly to the need to explicitly consider both the off-diagonal density matrix elements which describe the ESR transitions as well as the diagonal (and pseudodiagonal, cf. below) elements which relate to the spin state populations. But it is mainly due to the need to obtain fairly complete sets of the eigenvectors of the SLE, not just small sets of eigenvalues as in cw ESR. The computational challenges that result are therefore much greater than for cw ESR, especially if one hopes to have relatively fast algorithms which can permit nonlinear least-squares (NLLS) fitting to experiments. Such NLLS fitting often requires the computation of several hundred spectra as one iterates to a least-squares fit. Our considerable efforts at upgrading and adapting the computational algorithms for obtaining accurate eigenvalues and eigenvectors of the SLE to meet this challenge are described in Sec. III.

Several applications of the theory and their implications are discussed in Sec. IV. After a brief discussion of the general features of relaxation of "off-diagonal" and "diagonal" subspaces, we discuss how inhomogeneous broadening affects differently the two mirror-image coherence transfer pathways that are experimentally realized in COSY and 2D-ELDOR experiments. Although both are FID-based 2D signals, one is seen to be "echolike," whereas the other is simple "FID-like." When both are obtained in real experiments they provide complementary information to distinguish the different components that contribute to the inhomogeneous broadening, especially that due to the microscopic molecular ordering in complex fluids. These effects are illustrated with recent experiments. In addition, it is shown how the echolike component of the COSY signal may be utilized to provide the homogeneous linewidths across the ESR spectrum, and the conditions to optimize sensitivity to these widths are analyzed.

The ultraslow motional regime is considered in some detail. The relevant 2D-FT ESR experiments are necessarily echo based. It is first shown how these experiments can conveniently provide estimates of the very slow (1 μs and slower) rotational correlation times of viscous fluids (and of macromolecules) in accordance with the interpretations of Patyal *et al.* Special emphasis is given to the development of "rotational crosspeaks" in the 2D-ELDOR spectrum. Also discussed is how to use 2D-FT ESR to distinguish between the limiting models of very slow motional (SM) rates with little or no ordering vs that of very high ordering (HO) but substantial motional rates. Such models are typically virtually indistinguishable in cw ESR, but can be readily distinguished by 2D-ELDOR.

Finally, the role of nuclear modulation in the presence of residual motion is discussed. Given that 2D-FT ESR employs "hard" pulses that irradiate all allowed and forbidden ESR transitions, nuclear modulation is a characteristic feature of the spectra as long as the motion is not fast enough to average it out, as Patyal *et al.* have found. This feature is carefully analyzed, and it is also shown that nuclear modulation will arise even when motional rates are rapid provided there is substantial microscopic ordering. The nature of the modulation patterns is found to be different in the two cases of SM and HO, and this could, in principle, be utilized to better distinguish them.

A brief summary and conclusions appear in Sec. V.

II. THEORY

A. General formulation based on the stochastic Liouville equation

Molecules in fluids whose motional degrees of freedom may be treated as classical stochastic variables obeying a stationary Markov process and whose spin dynamics are treated quantum mechanically may be characterized by a density operator $\rho(\Omega,t)$ satisfying the stochastic Liouville equation of motion[8,9]

$$\frac{\partial}{\partial t}\rho(\Omega,t) = -i[\mathscr{H}(\Omega,t),\rho(\Omega,t)] - \Gamma(\Omega)[\rho(\Omega,t)-\rho_0(\Omega)], \quad (1)$$

where $\mathscr{H}(\Omega,t)$ is the spin Hamiltonian operator, which depends on the orientation of the molecule as specified by its Euler angles Ω, $\Gamma(\Omega)$ is the time-independent relaxation superoperator representing the motional processes frequently taken to be a Fokker–Planck operator, and $\rho_0(\Omega)$ is the equilibrium density operator.

In the absence of a microwave pulse, it is more convenient to use the reduced density operator $\chi(\Omega,t) = \rho(\Omega,t) - \rho_0(\Omega)$ to describe the relaxation toward thermal equilibrium, and Eq. (1) can be written as

$$\frac{\partial}{\partial t}\chi(\Omega,t) = -[i\mathscr{H}^{\times}(\Omega) + \Gamma(\Omega)]\chi(\Omega,t) \equiv -\mathscr{L}(\Omega)\chi(\Omega,t), \tag{2}$$

where $\mathscr{H}^{\times}(\Omega)$ is the commutator superoperator of the Hamiltonian and $\mathscr{L}(\Omega)$ is the stochastic Liouville operator. Then the formal solution of Eq. (2) can be written as

$$\chi(\Omega,t+t_0) = \exp(-\mathscr{L}t)\chi(\Omega,t_0) \tag{3}$$

and the evolution of the density matrix is fully described by the eigenmodes of the stochastic Liouville operator, which are obtained by diagonalizing a matrix representation of the stochastic Liouville operator.

In the presence of a microwave pulse, the Hamiltonian should include the effect of the pulse in the complete spin Hamiltonian as well as the relaxation. If the interaction with the pulse is much larger than the spin Hamiltonian terms in the appropriate rotating frame, then all the spins are uniformly affected by the pulse regardless of their resonance frequencies (i.e., the pulse is strong and nonselective). The duration of such an intense pulse is short, and the relaxation during the pulse can be ignored. Gorcester and Freed, and Patyal *et al.* demonstrated 2D-ESR experiments using pulses with 5 ns duration and ± 100 MHz nominal coverage, which provide good spectral coverage for ^{14}N (or ^{15}N) nitroxide samples at X band.[2,4,5] For simplicity of formulation, we will assume ideal nonselective pulses throughout this paper.[21] Then, ignoring the effects of the complete spin Hamiltonian and of relaxation during the pulses, the evolution of the density matrix can be expressed in terms of the pulse propagator superoperator $\mathscr{P}$ as follows:

$$\rho(t_0+t_p) = \mathscr{P}(t_p)\rho(t_0) \equiv P\rho(t_0)P^{-1}. \tag{4}$$

The evolution of the density matrix under an arbitrary pulse sequence is fully described by the stochastic Liouville operator and the pulse propagator as given in Eqs. (3) and (4).

To properly formulate the quantum mechanical properties of the spin Hamiltonian and the pulse propagator, and the classical motional processes that appear in the relaxation superoperator, it is most convenient to use spherical tensor operator formalism.[8,22,23] The formulation of the Liouville operator and of the pulse propagator is shown in the following sections. The explicit expressions will be given mainly for the case of a single electron spin and a single nuclear spin system, even though the formulation itself is general enough to include multiple quantum coherences from more than one equivalent spin.

1. The stochastic Liouville operator: Basis vectors

The basis states of the spin Hamiltonian for a single electron spin with spin quantum number S and magnetic quantum number m_S, may be written as $|S,m_S\rangle$ in Hilbert space. The basis for the Hamiltonian superoperator $\mathscr{H}^{\times}$ consists of the spin-state transitions, which are characterized by the initial and final magnetic quantum numbers, m_S' and m_S'', respectively. Each transition can be denoted by $|p^S,q^S\rangle$ where the two transition quantum numbers p^S and q^S are defined as

$$p^S = m_S'' - m_S', \quad q^S = m_S'' + m_S'. \tag{5}$$

The transition quantum number p^S defines the order of coherence associated with the density matrix element involved in the transition, and it plays an important role in distinguishing and characterizing the properties of the magnetic resonance signals. Note that we are using the ket form to represent the basis vectors in Liouville space, and they should be distinguished from the basis vectors in Hilbert space represented as rounded kets. This simple ket notation will be consistently used to specify the basis vectors in Liouville space throughout this paper.

One of the important sources of relaxation is the rotational diffusion process, which is most conveniently represented in terms of the Wigner rotation matrices $\mathscr{D}^L_{MK}(\Omega)$.[24] Therefore the basis vectors spanning the Liouville space suitable for describing the stochastic Liouville operator for a system of one electron spin ($S=1/2$) and one nuclear spin (I), are chosen to be the direct products of the spin transitions and the normalized Wigner rotation matrices[9,16]

$$|p^S,q^S,p^I,q^I;L,M,K\rangle \equiv |m_S',m_S'';m_I',m_I''\rangle \sqrt{\frac{2L+1}{8\pi^2}}\,\mathscr{D}^L_{MK}(\Omega), \tag{6}$$

where p^I, q^I are the transition quantum numbers for the nuclear spin defined in a similar manner to Eq. (5).

The basis vectors with different p^S indices are coupled only through the $\mathbf{S}_+$ or $\mathbf{S}_-$ operators, which appear only in the nonsecular terms in the spin Hamiltonian or in the interaction with the irradiating field as represented in the pulse propagator discussed in the next section. Therefore, in the high field limit where the nonsecular contributions are usually negligible (except for very fast motions), and in the absence of a pulse, the stochastic Liouville matrix is block diagonal in terms of the p^S indices, and one can diagonalize each p^S block separately to obtain the eigenmodes.

In typical ESR problems (a single electron spin, $S=1/2$), the $p^S=0$ basis vectors span the "diagonal subspace" (i.e., the collection of diagonal and pseudodiagonal density matrix elements for which $p^I=0$ and $p^I\neq 0$ respectively), and the $p^S=\pm 1$ basis vectors span two conjugate "off-diagonal subspaces." By solving for the respective sets of eigenvalues for the three subspaces, one obtains the eigenmodes that fully describe the evolution of the density matrix in the absence of any microwave pulse in the high field limit, i.e.,

$$O_1^{\mathrm{tr}}\mathscr{L}_1 O_1 = \Lambda_1, \quad O_0^{\mathrm{tr}}\mathscr{L}_0 O_0 = \Lambda_0, \quad O_{-1}^{\mathrm{tr}}\mathscr{L}_{-1} O_{-1} = \Lambda_{-1}. \tag{7}$$

Here the O and Λ matrices are respectively the orthogonal transformation matrix composed of the eigenvectors and the diagonal matrix of eigenvalues for each subspace with the p^S values for the subspace specified as a subscript. The detailed expressions for $\mathscr{L}$ and the properties of O and Λ will be discussed later (cf. Sec. II B).

2. Pulse propagator superoperator

The general expression for the pulse propagator in Eq. (4) can be obtained in terms of the spherical tensor operator basis.[22,23] The effect of the rotational transformation $R(\alpha,\beta,\gamma)$ corresponding to the three Euler angles (α,β,γ) on the spherical tensor operator is

$$\mathscr{R}(\alpha,\beta,\gamma)T_{lm}=R(\alpha,\beta,\gamma)T_{lm}R^{-1}(\alpha,\beta,\gamma)$$
$$=\sum_{m'} T_{lm'}\mathscr{D}^{l}_{m'm}(\alpha,\beta,\gamma), \tag{8}$$

where T_{lm} is the irreducible tensor operator of rank l and component m. The rotation operator for the microwave pulse with a tipping angle θ and phase ϕ can be decomposed into three consecutive rotations to achieve the standard phase conventions[25] as follows:

$$R=e^{-i\phi S_z}e^{-i\theta S_x}e^{i\phi S_z}=e^{i(\pi/2-\phi)S_z}e^{-i\theta S_y}e^{-i(\pi/2-\phi)S_z}. \tag{9}$$

Then the pulse propagator superoperator can be written as[23]

$$\mathscr{P}(\theta,\phi)T_{lm}=\sum_{m'} T_{lm'}\mathscr{D}^{l}_{m'm}\left(-\frac{\pi}{2}+\phi,\theta,\frac{\pi}{2}-\phi\right). \tag{10}$$

For the case of a single electron spin system ($S=1/2$), the density operator can be expanded in terms of the irreducible tensor operators T_{lm} of rank 0 and 1. The irreducible tensor operator T_{00} merely refers to the population conservation (i.e., it is the unit operator), and the irreducible tensor operator T_{10} specifies the polarization. The irreducible tensor operators $T_{1\pm1}$ are the two counter-rotating single-transition shift operators. Writing the pulse propagator superoperator $\mathscr{P}$ in the $|p^S,q^S\rangle$ basis, we obtain the following expression:

$$\mathscr{P}=\begin{array}{c}\begin{matrix}\quad|0,1\rangle & |0,-1\rangle & |1,0\rangle & |-1,0\rangle\end{matrix}\\ \begin{pmatrix}\cos^2(\theta/2) & \sin^2(\theta/2) & i/2\sin\theta\, e^{i\phi} & -i/2\sin\theta\, e^{-i\phi}\\ \sin^2(\theta/2) & \cos^2(\theta/2) & -i/2\sin\theta\, e^{i\phi} & i/2\sin\theta\, e^{-i\phi}\\ i/2\sin\theta\, e^{-i\phi} & -i/2\sin\theta\, e^{-i\phi} & \cos^2(\theta/2) & \sin^2(\theta/2)e^{-i2\phi}\\ -i/2\sin\theta\, e^{i\phi} & i/2\sin\theta\, e^{i\phi} & \sin^2(\theta/2)e^{i2\phi} & \cos^2(\theta/2)\end{pmatrix}\end{array}. \tag{11}$$

Each element $\langle p_1^S,q_1^S|\mathscr{P}|p_2^S,q_2^S\rangle$ is seen to depend on $\exp(-i\Delta p^S\phi)$ where $\Delta p^S=p_1^S-p_2^S$. Therefore, each coherence transfer pathway has a distinct dependence on the phase of the pulse, which enables one to remove unwanted signals by phase cycling. Note that the pulse propagator is independent of all quantum numbers which appear in the Liouville space representation of Eq. (6) except for p^S and q^S.

3. Coherence transfer pathways and the 2D-ESR signal

Given Eqs. (7) and (11), it is straightforward to calculate the 2D-ESR signal for various types of experiments. The initial density matrix is the equilibrium density matrix which has nonzero elements only for zeroth-order coherence ($p^S=0$). The spins in the xy plane immediately after a $\pi/2$ pulse are of first-order coherence. They will be represented as *transition moment vectors* $|v_1\rangle$ and $|v_{-1}\rangle$, specifying the two counter-rotating components of the magnetization which are represented by the off-diagonal density matrix elements corresponding to $p^S=\pm1$. In simulating the cw ESR spectra, the *starting vector* for the Lanczos or conjugate gradient (CG) algorithms is taken as $|v_1\rangle$.[16] During the detection period, only the density matrix elements with $p^S=-1$ contribute to observable magnetization $\langle \mathbf{S}_+\rangle$. The 2D-ESR signal for the coherence transfer pathway of interest can be written as a

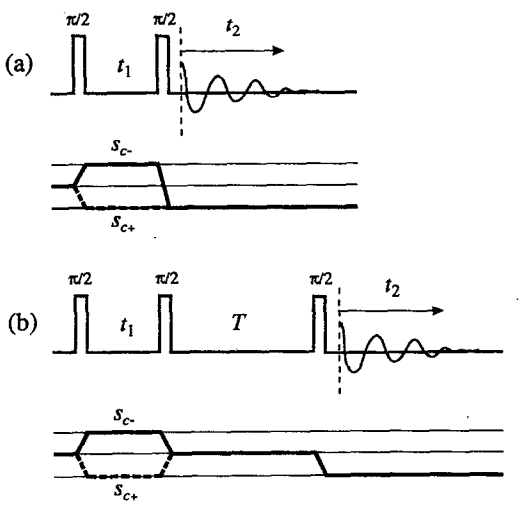

FIG. 1. Pulse sequences and coherence pathway diagram for the (a) COSY sequence and (b) 2D-ELDOR sequence. The solid and the dashed lines in the coherence pathway diagram represent the S_{c-} and the S_{c+} signals, respectively. SECSY and echo-ELDOR signals are obtained by delaying data acquisition by t_1 and the S_{c-} is the corresponding coherence pathway to form the echo.

product involving the exponentiated eigenvalue matrix, the eigenvector matrix, the pulse propagator matrix, and the transition moment vectors as we show in the next paragraphs. The pulse sequences and the coherence transfer pathways for the experiments considered in this paper are summarized in Fig. 1.

The coherence transfer pathway for a simple FID is $p^S=0\rightarrow-1$. Using Eqs. (3) and (7), the signal can be written as

$$\begin{aligned} S^{\mathrm{FID}}&=\langle v_{-1}|e^{-\mathscr{L}t_1}|v_{-1}\rangle \\ &=\langle v_{-1}|O_{-1}O_{-1}^{\mathrm{tr}}e^{-\mathscr{L}t_1}O_{-1}O_{-1}^{\mathrm{tr}}|v_{-1}\rangle \\ &=\langle v_{-1}|O_{-1}e^{-\Lambda_{-1}t_1}O_{-1}^{\mathrm{tr}}|v_{-1}\rangle. \end{aligned} \tag{12}$$

Even though Eq. (3) describes the evolution of the density matrix in terms of the reduced density matrix $\chi=\rho-\rho_{\mathrm{eq}}$, the interconversion between ρ and χ is not necessary here since $\rho_{\mathrm{eq}}=0$ in the off-diagonal space. The orthonormal property of the transformation matrix O is used in Eq. (12). Note that the ith component of the vector $O_{-1}^{tr}|v_{-1}\rangle$ is the projection of the ith eigenvector on the transition moment vector $|v_{-1}\rangle$. Therefore the eigenvalues and the "weighting factors" (i.e., the squares of the projections) of the eigenmodes determine the FID (or alternatively the cw spectrum) completely. The weighting factors are readily available without calculating eigenvectors explicitly, and this is fully utilized in the simulation of the cw ESR spectra.[9,10,16]

In the COSY sequence, the coherence transfer pathways $p^S=0\rightarrow\mp1\rightarrow-1$ are responsible for the S_{c+} and S_{c-} signals [which are referred to as "P-type" and "N-type" signals in nuclear magnetic resonance (NMR)] defined by Gamliel and Freed,[25] respectively. Those signals can be written as

$$\begin{aligned} S_{c\pm}^{\mathrm{COSY}}=&\langle v_{-1}|O_{-1}e^{-\Lambda_{-1}t_2}O_{-1}^{\mathrm{tr}}P_{(-1\leftarrow\mp1)} \\ &\times O_{\mp1}e^{-\Lambda_{\mp1}t_1}O_{\mp1}^{\mathrm{tr}}|v_{\mp1}\rangle, \end{aligned} \tag{13}$$

where $P_{(p_2^S\leftarrow p_1^S)}$ denotes the pulse propagator that transforms the density matrix elements in the p_1^S subspace into the density matrix elements in the p_2^S subspace. The pulse propagators $P_{(p_2^S\leftarrow p_1^S)}$ in Eq. (13) are proportional to the unit matrix [cf. Eq. (11)].

The coherence transfer pathways for the 2D-ELDOR sequence can be written as $p^S=0\rightarrow\mp1\rightarrow0\rightarrow-1$ for the $S_{c\pm}$ signals. Concentrating only on the portion of the density matrix that follows this coherence transfer pathway up to and just before the third pulse (i.e., $p^S=0\rightarrow\mp1\rightarrow0$), we have

$$\begin{aligned} \rho(t_1,T)=&O_0e^{-\Lambda_0T}O_0^{\mathrm{tr}}(P_{(0\leftarrow\mp1)}O_{\mp1}e^{-\Lambda_{\mp1}t_1}O_{\mp1}^{\mathrm{tr}}|v_{\mp1}\rangle \\ &-\rho_{\mathrm{eq}})+\rho_{\mathrm{eq}} \\ =&O_0e^{-\Lambda_0T}O_0^{\mathrm{tr}}P_{(0\leftarrow\mp1)}O_{\mp1}e^{-\Lambda_{\mp1}t_1}O_{\mp1}^{\mathrm{tr}}|v_{\mp1}\rangle \\ &+(1-O_0e^{-\Lambda_0T}O_0^{\mathrm{tr}})\rho_{\mathrm{eq}}. \end{aligned} \tag{14}$$

Note that the equilibrium density matrix ρ_{eq} which arises from the interconversion between ρ and χ cannot be ignored in the diagonal space of $p^S=0$. Those terms involving ρ_{eq} are independent of t_1, and appear along $\omega_1=0$ (i.e., they are axial M terms).[2] They are suppressed by phase cycling since they do not depend on the phase of the first pulse.[25] Then the 2D-ELDOR signal following the third pulse can be written as

$$S_{c\pm}^{\mathrm{ELDOR}}=\langle v_{-1}|O_{-1}e^{-\Lambda_{-1}t_2}O_{-1}^{\mathrm{tr}}P_{(-1\leftarrow0)}O_0e^{-\Lambda_0T}O_0^{\mathrm{tr}}P_{(0\leftarrow\mp1)}O_{\mp1}e^{-\Lambda_{\mp1}t_1}O_{\mp1}^{\mathrm{tr}}|v_{\mp1}\rangle. \tag{15}$$

The pulse propagators between the diagonal space and the off-diagonal space are rectangular matrices [cf. Eq. (11)]. Now the problem reduces to one of obtaining the eigenvalues and eigenvectors for the stochastic Liouville matrix.

B. Symmetrization of the stochastic Liouville matrix

The detailed expression for the spin Hamiltonian superoperator in the basis set of $|p^S,q^S,p^I,q^I;L,,M,K\rangle$ as defined in Eq. (6) is summarized in Appendix A. It was shown that this stochastic Liouville matrix can be reduced to a complex symmetric form by expressing it in a new basis set defined as[9,16]

$$|p^S,q^S,p^I,q^I;L,M,K,j^K\rangle_K=[2(1+\delta_{K,0})]^{-1/2}(j^K)^{1/2}|p^S,q^S,p^I,q^I\rangle\otimes(|L,M,K\rangle+j^K(-1)^{L+K}|L,M,-K\rangle), \tag{16}$$

where the K index now has only non-negative values, and the allowed values for j^K are

$$j^K=\begin{cases}(-1)^L & \text{for } K=0\\ \pm1 & \text{for } K>0\end{cases}. \tag{17}$$

Note that the subscript K is used to specify basis vectors in the "K-symmetrized basis." The matrix elements of the Liouville operator and its symmetry properties for different types of ESR problems in this K-symmetrized basis set are described by Meirovitch *et al.*[16]

The transformation given in Eq. (16) reflects a fundamental symmetry of the basis set, namely the parity of the basis kets with respect to the $\mathbf{C}_2(y)$ operator which performs a π rotation about the y axis of the diffusion frame.[26] Specifically, in the original basis, $\mathbf{C}_2(y)|L,M,K\rangle=(-1)^{L+K}|L,M,-K\rangle$, which may be substituted into Eq. (16) to show that $\mathbf{C}_2(y)|L,M,K,j^K\rangle=j^K|L,M,K,j^K\rangle$. Thus, each vector in the K-symmetrized basis is an eigenfunction of the $\mathbf{C}_2(y)$ operator, and the index j^K is its corresponding eigenvalue, or parity. The additional factor of i for the basis

vectors with $j^K=-1$ is included in Eq. (16) in order to convert the stochastic Liouville operator to a complex symmetric form.

In the high field approximation, and for motions that are not extremely fast, we can ignore the contribution of the nonsecular terms in the Hamiltonian, which results in a decoupling of the three subspaces as already noted. In this case, it is possible to take advantage of additional symmetries in both the diagonal and the off-diagonal subspaces. For the *off-diagonal* subspaces, the following symmetrization may be used:[16]

$$|\pm 1,0,p^I,q^I;L,M,K,j^K,j^M\rangle_{KM}$$

$$=[2(1+\delta_{M,0}\delta_{p^I,0})]^{-1/2}(|\pm 1,0,p^I,q^I;L,M,K,j^K\rangle_K + j^M(-1)^{L+M}|\pm 1,0,-p^I,q^I;L,-M,K,j^K\rangle_K), \quad (18)$$

where the M index has only non-negative values (if $M=0$, the index p^I is also non-negative), and the allowed values for j^M are

$$j^M=\begin{cases}(-1)^L & \text{for } p^I=M=0\\ \pm 1 & \text{otherwise}\end{cases}. \quad (19)$$

The Liouville operator matrix elements in this "M-symmetrized" off-diagonal basis, including the nuclear Zeeman interaction, are

$$\begin{aligned}&\langle \pm 1,0,p_1^I,q_1^I;L_1,M_1,K_1,j_1^K,j_1^M|\mathscr{H}^\times|\pm 1,0,p_2^I,q_2^I;L_2,M_2,K_2,j_2^K,j_2^M\rangle_{KM}\\ &=N_L(L_1,L_2)N_K(K_1,K_2)N_p(p_1^I,M_1;p_2^I,M_2)(-1)^{M_1+K_1}\Bigg\{\delta_{j_1^M,j_2^M}\sum_{\mu=g,A,l}R_{\mu,l}(L_1,K_1,j_1^K;L_2,K_2,j_2^K)\\ &\times\Bigg[\langle \pm 1,0,p_1^I,q_1^I|A_{\mu,L}^{(l,p_1^I-p_2^I)^\times}|\pm 1,0,p_2^I,q_2^I\rangle d^l_{p_1^I-p_2^I,M_1-M_2}(\psi)\begin{pmatrix}L_1 & l & L_2\\ M_1 & M_2-M_1 & -M_2\end{pmatrix}\\ &+j_2^M(-1)^{L_2+M_2}\langle \pm 1,0,p_1^I,q_1^I|A_{\mu,L}^{(l,p_1^I+p_2^I)^\times}|\pm 1,0,p_2^I,q_2^I\rangle d^l_{p_1^I+p_2^I,M_1+M_2}(\psi)\begin{pmatrix}L_1 & l & L_2\\ M_1 & -M_1-M_2 & M_2\end{pmatrix}\Bigg]\\ &+(1-\delta_{j_1^M,j_2^M})\delta_{j_1^K,j_2^K}\delta_{p_1^S,p_2^S}\delta_{q_1^S,q_2^S}\delta_{p_1^I,p_2^I}\delta_{q_1^I,q_2^I}\delta_{L_1,L_2}\delta_{M_1,M_2}\delta_{K_1,K_2}\frac{g_N\beta_N B_0}{\hbar}p_1^I\Bigg\}, \end{aligned} \quad (20)$$

where

$$\begin{aligned}R_{\mu,l}(L_1,K_1,j_1^K;L_2,K_2,j_2^K)&=\begin{pmatrix}L_1 & l & L_2\\ K_1 & K_2-K_1 & -K_2\end{pmatrix}G_{\mu,l}(j_1^K,j_2^K;K_1-K_2)\\ &+j_2^K(-1)^{L_2+K_2}\begin{pmatrix}L_1 & l & L_2\\ K_1 & -K_1-K_2 & K_2\end{pmatrix}G_{\mu,l}(j_1^K,j_2^K;K_1+K_2)\end{aligned} \quad (21)$$

and the quantities $G_{\mu,l}$ are defined as

$$\begin{aligned}G_{\mu,l}(j_1^K,j_2^K;K)&=\delta_{j_1^K,j_2^K}\,\mathrm{Re}\{F_{\mu,D}^{(l,K)}\}\\ &+(1-\delta_{j_1^K,j_2^K})j_1^K\,\mathrm{Im}\{F_{\mu,D}^{(l,K)}\}.\end{aligned} \quad (22)$$

The normalization factors are defined as

$$\begin{aligned}N_L(L_1,L_2)&=(2L_1+1)^{1/2}(2L_2+1)^{1/2},\\ N_K(K_1,K_2)&=(1+\delta_{K_1,0})^{-1/2}(1+\delta_{K_2,0})^{-1/2},\\ N_p(p_1^I,M_1;p_2^I,M_2)&=[(1+\delta_{p_1^I,0}\delta_{M_1,0})\\ &\times(1+\delta_{p_2^I,0}\delta_{M_2,0})]^{-1/2}\end{aligned} \quad (23)$$

and all the other quantities are defined in Appendix A.

The relaxation superoperator is block diagonal with respect to both j^K and j^M, and its matrix elements in the M-symmetrized basis are given in Appendix B. The starting vector, also given in Appendix B, has nonvanishing elements only for $j^K=1$ and $j^M=1$.

A careful analysis shows that an equivalent symmetrization to Eq. (18) exists for the *diagonal* subspace, which can be written as

$$|0,1,p^I,q^I;L,M,K,j^K,j^M\rangle_{KM}$$

$$=\frac{1}{\sqrt{2}}(|0,1,p^I,q^I;L,M,K,j^K\rangle_K - j^M(-1)^{L+M}|0,-1,-p^I,q^I;L,-M,K,j^K\rangle_K). \quad (24)$$

This symmetrization differs from that used for the off-diagonal space in that (i) the linear combinations are taken with respect to q^S as well as M and p^I; (ii) the index j^M can be ± 1 *regardless* of the other indices, and (iii) the index M after the symmetrization *may* be a negative number. How-

ever, we shall still refer to Eq. (24) as "M symmetrization" since it has a very close relationship to the M symmetrization in the off-diagonal space.

When $p^I=0$, the basis vectors $|0,\pm 1,0,q^I,\cdots\rangle_K$ on the right-hand side of Eq. (24) represent the population of the spin states with $m_I=q^I/2$ and $m_S=\pm 1/2$. Then the difference between the populations corresponding to the two basis vectors with $q^S=\pm 1$ is proportional to the polarization, which relaxes with the characteristic longitudinal relaxation time, T_1. The sum of these two populations does not change with time (i.e., total population is conserved) in the absence of cross relaxation.

The Liouville matrix elements for the M-symmetrized basis in the diagonal space are given by

$$\begin{aligned}
&\langle 0,1,p_1^I,q_1^I;L_1,M_1,K_1,j_1^K,j_1^M|\mathscr{H}^\times|0,1,p_2^I,q_2^I;L_2,M_2,K_2,j_2^K,j_2^M\rangle_{KM}\\
&\quad=N_L(L_1,L_2)N_K(K_1,K_2)(-1)^{M_1+K_1}\Bigg[\delta_{j_1^M,j_2^M}\sum_{\mu=g,A,I}R_{\mu,I}(L_1,K_1,j_1^K;L_2,K_2,j_2^K)\\
&\qquad\times\langle 0,1,p_1^I,q_1^I|A_{\mu,L}^{(I,p_1^I-p_2^I)^\times}|0,1,p_2^I,q_2^I\rangle d^I_{p_1^I-p_2^I,M_1-M_2}(\psi)\begin{pmatrix}L_1 & I & L_2\\ M_1 & M_2-M_1 & -M_2\end{pmatrix}\\
&\qquad+(1-\delta_{j_1^M,j_2^M})\delta_{j_1^K,j_2^K}\delta_{p_1^S,p_2^S}\delta_{q_1^S,q_2^S}\delta_{p_1^I,p_2^I}\delta_{q_1^I,q_2^I}\delta_{L_1,L_2}\delta_{M_1,M_2}\delta_{K_1,K_2}\frac{g_N\beta_N B_0}{\hbar}p_1^I\Bigg].
\end{aligned}\tag{25}$$

Unlike the elements for the off-diagonal space, there is no term with $p_1^I+p_2^I$ for the diagonal space, since $\langle 0,1,p_1^I,p_2^I|A_{\mu,L}^{I(p_1^I+p_2^I)^\times}|0,-1,p_1^I,p_2^I\rangle=0$ in the original basis for all interactions (cf. Appendix A). The expressions for the relaxation superoperator are given in Appendix B, and they are factored with respect to j^M in the diagonal subspace.

In the M-symmetrized basis, the pulse propagator that converts the off-diagonal basis set into the diagonal basis set can be shown to be

$$\begin{aligned}
&\mathscr{P}_{(p^S=0)\leftarrow(|p^S|=1)}|\pm 1,0,p^I,q^I;L,M,K,j^K,j^M\rangle_{KM}\\
&\quad=\pm(1+\delta_{p^I,0}\delta_{M,0})^{-1/2}\{|0,1,p^I,q^I;L,M,K,j^K,j^M\rangle_{KM}+j^M(-1)^{L+M}|0,1,-p^I,q^I;L,-M,K,j^K,j^M\rangle_{KM}\}.
\end{aligned}\tag{26}$$

The pulse propagator from the diagonal space to off-diagonal space is

$$\begin{aligned}
&\mathscr{P}_{(|p^S|=1)\leftarrow(p^S=0)}|0,1,p^I,q^I;L,M,K,j^K,j^M\rangle\\
&\quad=\begin{cases}(1+\delta_{M,0}\delta_{p^I,0})^{1/2}(|1,0,p^I,q^I;L,M,K,j^K,j^M\rangle-|-1,0,p^I,q^I;L,M,K,j^K,j^M\rangle) & \text{if } M\geq 0\\ j^M(-1)^{L+M}(|1,0,-p^I,q^I;L,-M,K,j^K,j^M\rangle-|-1,0,-p^I,q^I;L,-M,K,j^K,j^M\rangle) & \text{if } M<0.\end{cases}
\end{aligned}\tag{27}$$

The pulse propagator from the $p^S=1$ space to the $p^S=-1$ space, which appears in the COSY experiment, is a unit matrix. Equations (26) and (27) show that the pulse propagator maintains the symmetry defined by the j^M index (i.e., j^M is unchanged when the pulse propagator transforms a diagonal basis vector into an off-diagonal basis vector).

In the absence of the nuclear Zeeman term and for high fields, one needs to solve the stochastic Liouville equation in the off-diagonal space only for the $j^M=1$ subspace. This is valid since (i) the transition moment vector (i.e., the density matrix right after the first pulse) only has nonzero components for $j^M=1$, (ii) the pulse propagator keeps the j^M symmetry, and (iii) the stochastic Liouville matrix is block diagonal with respect to j^M. Furthermore, the two off-diagonal subspaces are complex conjugates, so that $O_{-1}=O_1^*$, $\Lambda_{-1}=\Lambda_1^*$. Therefore one needs to diagonalize only one of them, which significantly improves the computational efficiency.

In cases where the nuclear Zeeman interaction is important, it is necessary to include basis vectors with $j^M=-1$, since the nuclear Zeeman terms appear off-diagonal with respect to j^M [note the terms with $1-\delta_{j_1^M,j_2^M}$ in Eqs. (20) and (25)], in contrast to the other terms in the stochastic Liouville operator (g tensor, hyperfine tensor, diffusion tensor) and in the starting vector. The nuclear Zeeman term also causes the eigenvalues and eigenvectors of the two off-diagonal spaces to deviate from the simple complex conjugate relations ($O_{-1}=O_1^*$, $\Lambda_{-1}=\Lambda_1^*$), which is the source, from a mathematical viewpoint, of the nuclear modulation of the echo. Therefore it is necessary to diagonalize both off-diagonal spaces separately to calculate the S_{c-} COSY or ELDOR spectra.

III. COMPUTATIONAL ALGORITHMS

The stochastic Liouville matrix can always be represented as a complex symmetric, but not Hermitian, matrix[11] when both the spin Hamiltonian superoperator $\mathscr{H}^\times$ and the relaxation operator Γ are included. It is usually a very large

and sparse matrix and is diagonalized by a complex orthogonal transformation as indicated in Eq. (7). Methods for diagonalizing complex symmetric matrices are reviewed by Schneider and Freed for simulating the cw ESR spectra.[11] In the calculation of FIDs or cw spectra, weighting factors are obtained by monitoring projections of the eigenvectors on the transition moment vector [cf. Eq. (12)], and explicit calculation of the eigenvectors is not necessary. For simulating 2D-ESR spectra, however, the eigenvectors are usually required, as implied in Eqs. (13) and (15), which requires a significantly more intensive calculation and larger storage space.

Simulation of the 2D-ESR spectra becomes more difficult when the diagonal subspace is involved in the coherence transfer pathway as in the 2D-ELDOR experiment. Without taking any symmetry properties into account, the dimension of the diagonal subspace is twice that of the off-diagonal subspace. The diagonalization of such large matrices is challenging even with modern computers, so it is necessary to minimize the dimension of the matrix by keeping only the relevant basis vectors.

Another difficulty in dealing with the diagonal subspace is the fact that there is no single transition moment vector (or "starting vector") that can be relied on to project out all the relevant eigenmodes. For instance, the vector $|v_0\rangle$ produced by a π pulse on the equilibrium density operator lacks any projection on the subspace spanned by the pseudodiagonal basis vectors, which are introduced through the action of $\mathscr{H}^{\times}$ during the evolution period, and which do play an important role in the development of crosspeaks in the 2D-ELDOR spectrum. In the off-diagonal space, the density matrix obtained by applying a $\pi/2$ pulse on the equilibrium density matrix defines the magnetization at the start of the evolution period, and the eigenmodes that do not have any significant projection on that density matrix are unimportant. The natural extension of the strategy above would be to define a set of starting vectors as a collection of diagonal density matrices each of which is the off-diagonal density matrix after a particular evolution time t_1 premultiplied by the pulse propagator $P_{(0\leftarrow\pm 1)}$. Note that the vector $|v_0\rangle$ would be one of the starting vectors corresponding to $t_1=0$. The starting vectors for the diagonal space can be written as

$$|u_{\mp 1}(t_1)\rangle = P_{(0\leftarrow\mp 1)} O_{\mp 1} e^{-\Lambda_{\mp 1} t_1} O_{\mp 1}^{\mathrm{tr}} |v_{\mp 1}\rangle. \tag{28}$$

The implementation of multiple starting vectors for the diagonal space allows two different methods for calculating the 2D-ELDOR signal.

The explicit calculation of the eigenvectors followed by spectral simulation using Eq. (15) is the most obvious and general way. This method has the advantage that one can simulate 2D-ESR spectra from any pulse sequence since all the relevant eigenvalues and eigenvectors are already known. If the coherence transfer pathway before and after the diagonal subspace are either 1 or -1 as in the 2D-ELDOR sequence, and one is interested in the final spectrum instead of the eigenvectors themselves, the storage space for the eigenvectors of the diagonal space can be reduced by about a factor of 2 by storing the product of the eigenvectors and the pulse propagator that transforms the diagonal subspace into the off-diagonal space [i.e., the $P_{(\pm 1\leftarrow 0)}O_0$ matrix in Eq. (15)], because the pulse propagator $P_{(\pm 1\leftarrow 0)}O_0$ is a rectangular matrix of dimension $n_1\times n_0$, where n_1, n_0 are the dimensions of the off-diagonal and the diagonal subspaces, respectively. One can further reduce the space by storing only the eigenvectors that have significant projection on the starting vectors.

The alternative method is an extension of the strategy used in the simulation of the cw ESR spectrum. Using Eq. (28), the 2D-ELDOR signal in Eq. (15) can be written as

$$S_{c\pm}^{\mathrm{ELDOR}} = \langle u_{-1}(t_2)| O_0 e^{-\Lambda_0 T} O_0^{\mathrm{tr}} |u_{\mp 1}(t_1)\rangle. \tag{29}$$

This can be regarded as evaluation of the cross correlation of $|u(t_1)\rangle$ and $|u(t_2)\rangle$ for each set of values of (t_1,t_2). Note that $O_0^{\mathrm{tr}}|u(t)\rangle$ is the projection of the eigenvectors on the starting vector $|u(t)\rangle$, which may be obtained without calculating the eigenvectors explicitly. This approach requires less storage space even though the computational efficiency depends on the algorithm used.

The following subsections will describe various aspects of the algorithms that we have used in simulating 2D-ESR spectrum.

A. The Lanczos algorithm (LA)

The Lanczos and related algorithms are known to be very efficient in dealing with large sparse matrices. They take full advantage of the sparsity of the matrices in both storage and computation, which has made them ideal for calculating cw ESR spectra.[9,11] The computational efficiency is proportional to $nn_l n_s$ where n, n_l, and n_s are the dimension of the matrix, the number of Lanczos steps, and the average number of nonzero elements in a row of the matrix, respectively. However, one major drawback of the LA is its loss of orthogonality amongst the Lanczos vectors due to numerical roundoff errors. Methods to circumvent this problem via complete or selective reorthogonalization are described by Golub and references therein.[27]

The eigenvectors of the tridiagonal matrix produced by the LA can be obtained by inverse iteration or by QR factorization.[28] They can be transformed to the eigenvectors expressed in the basis of the original matrix using the set of Lanczos vectors obtained in the process of tridiagonalization. However, a more preferable method based on the conjugate gradient method is described below (cf. Sec. III B).

The Lanczos and related algorithms inherently require a starting vector. Given a physically relevant starting vector, the LA projects out very rapidly those eigenmodes with a significant projection on the starting vector. This has been one of the main advantages of the LA. It was pointed out above [cf. Eq. (28)] that one really has multiple starting vectors for the diagonal space. We find, however, that a single linear combination of starting vectors generated by Eq. (28) for the first five steps in t_1 used in the experiment constitutes a satisfactory starting vector.

Unlike cw ESR cases, 2D-ESR simulations can require a fairly complete set of good eigenvalues. In such cases, the Lanczos projections can be continued for as much as 2–5 times the dimension of the original matrix in order to achieve this, but then one has to deal with removing spurious and

duplicate eigenvalues. Cullum and Willoughby suggested a method of identifying spurious eigenvalues by comparing the eigenvalues of the tridiagonal matrix $\hat{T}_m$ of dimension m and those of another tridiagonal matrix obtained from $\hat{T}_m$ by deleting the first row and the first column of $\hat{T}_m$.[28] This works fairly well if the eigenvalues are well separated, which is the case in the fast motional regime. As the motion slows down, the eigenvalues get closer to each other, and the number of eigenmodes with significant projection on the starting vector increases. Near the rigid limit where the eigenvalues are almost continuous, it is difficult to discern small but real differences from differences due to numerical roundoff error. Thus it becomes extremely difficult to adjust the tolerance needed to identify the duplicate and spurious eigenvalues without eliminating some good eigenvalues. This happens more often in the diagonal subspace where many important eigenvalues are closely located along the real axis.

One general and objective test to determine how good is the set of eigenvalues and eigenvectors in the diagonal subspace is the fact that the 2D-ELDOR spectrum at zero mixing time is equivalent to the COSY spectrum as implied in Eqs. (13) and (15). This is the test for the equality $O_0 O_0^{\mathrm{tr}}=\mathbf{1}$, which ensures the orthogonality between eigenvectors. However, this criterion may be too stringent considering that (i) the eigenmodes with large real parts (fast decaying components) remain important only for small mixing times, and (ii) the spectrum for mixing times less than 40 ns cannot be obtained in the laboratory due to spectrometer dead times. But we find this conservative criterion guarantees the reliability of the eigenvectors of the diagonal space.

Numerical experiments show that the plain LA without the spurious eigenvalue test or reorthogonalization produces good eigenvalues and eigenvectors (by inverse iteration) when the rotational diffusion coefficient is $R \gtrsim 10^7\ \mathrm{s}^{-1}$ for nitroxides at conventional X-band frequencies. Using the spurious eigenvalue test makes the procedure more stable and the method can be used up to $R \gtrsim 10^6\ \mathrm{s}^{-1}$. For motional rates slower than $R=10^6\ \mathrm{s}^{-1}$, the test in its present form becomes uncertain and other methods that enforce the orthogonality need to be introduced.

B. The conjugate gradient (CG) algorithm and projection of the eigenvectors

The CG algorithm designed for solving linear equations has actually been shown to provide a diagonalization method that is equivalent to the LA.[11,27] It has the advantage that an objective criterion for convergence in the number of Lanczos steps can be monitored with a small amount of extra computational work. Our most successful version for simulating 2D-FT ESR spectra that is based on the LA, actually uses the CG version, as described by Vasavada *et al.*[12] for calculating eigenvalues. One can then use the inverse iteration approach to obtain eigenvectors as in the LA. In this mode, we find the spectral simulations are at least an order of magnitude faster than more conventional procedures, such as the Rutishauser algorithm (cf. Sec. III C), but it is restricted to $R \gtrsim 10^6\ \mathrm{s}^{-1}$ for nitroxides (at X band) as we have noted. That is, the CG algorithm also suffers from the loss of orthogonality between Lanczos vectors.

There is an important variation of the CG algorithm which can be utilized for calculating each eigenvector corresponding to a known eigenvalue. The basic CG algorithm is an iterative method that solves a linear equation $\mathbf{A}\cdot\mathbf{x}=\mathbf{b}$ for a square matrix $\mathbf{A}$ of dimension n and a vector $\mathbf{b}$.[29] The CG algorithm can be applied to solve the following linear equation:

$$\mathbf{A}'\cdot\mathbf{x}'=\mathbf{b}', \quad \text{where } \mathbf{A}'=\mathbf{A}-\lambda\mathbf{I}+s\mathbf{I}, \ \mathbf{b}'=s\mathbf{b}. \tag{30}$$

The new matrix $\mathbf{A}'$ is obtained by subtracting $(\lambda-s)$ multiplied by a unit matrix $\mathbf{I}$, where λ is one of the eigenvalues of $\mathbf{A}$, and s is a small shift parameter added so as not to divide by zero [cf. Eq. (31)]. Notice that Eq. (30) reduces to the eigenvalue equation $(\mathbf{A}-\lambda\mathbf{I})\mathbf{x}=0$ in the limit of $s\to 0$. We will show that the new solution vector $\mathbf{x}'$ is the eigenvector corresponding to the eigenvalue λ when certain conditions are satisfied. The solution vector $\mathbf{x}'$ depends on both λ and s and may be written formally as

$$\mathbf{x}'=\frac{s}{(s-\lambda)\mathbf{I}+\mathbf{A}}\,\mathbf{b}=\mathbf{O}\,\frac{s}{(s-\lambda)\mathbf{I}+\Lambda}\,\mathbf{O}^{\mathrm{tr}}\mathbf{b}, \tag{31}$$

where Λ and $\mathbf{O}$ are the matrices that contain the eigenvalues and eigenvectors of $\mathbf{A}$, respectively. The eigenvector matrix is a collection of eigenvectors and may be written as $(\mathbf{q}_1,\mathbf{q}_2,\ldots,\mathbf{q}_n)$ where $\mathbf{q}_j$ represents the jth eigenvector of $\mathbf{A}$. Expanding the matrix multiplication in Eq. (31), the ith element of $\mathbf{x}'$ can be shown to be

$$(\mathbf{x}')_i=\sum_{j=1}^{n}\left(\frac{s}{s+(\lambda_j-\lambda)}\right)(\mathbf{q}_j^{\mathrm{tr}}\cdot\mathbf{b})(\mathbf{q}_j)_i$$

$$\xrightarrow[\text{for all } \lambda_j\neq\lambda]{(\lambda_j-\lambda)\gg s} (\mathbf{q}_\lambda^{\mathrm{tr}}\cdot\mathbf{b})(\mathbf{q}_\lambda)_i. \tag{32}$$

Choosing the shift parameter s much smaller than the separation between the eigenvalues, the summation is dominated by the eigenvector $\mathbf{q}_\lambda$ corresponding to that eigenvalue $\lambda_j\approx\lambda$ for which $|\lambda_j-\lambda|\ll s$. Therefore the solution vector $\mathbf{x}'$ is proportional to $\mathbf{q}_\lambda$ as long as the starting vector $\mathbf{b}$ has a non-negligible projection on $\mathbf{q}_\lambda$. Once the approximate eigenvector is obtained, the whole procedure may be repeated using the solution vector as the starting vector if a more accurate eigenvector is desired. We find that this method proves to be very stable, and it retains all the merits of the LA for large sparse matrices. (One should use as $\mathbf{b}$ the linear combination starting vector referred to in Sec. III A.) It can also be easily parallelized to improve the computational efficiency since the eigenvector calculations are completely independent. This should be the method of choice when the eigenvalues are known (e.g., from the LA or Rutishauser algorithm) and the eigenvectors are required. We find it is more reliable than the more conventional approaches of inverse iteration or QR factorization following the Lanczos tridiagonalization procedure.[28,30] This becomes important for cases where $R \lesssim 10^{-6}\ \mathrm{s}^{-1}$ (for nitroxides at X band).

C. The Rutishauser algorithm (RA)

The RA, a variant of the Givens method was introduced to the magnetic resonance community by the work of Gordon and Messenger.[31] Unlike the Lanczos-based iterative methods, the Rutishauser tridiagonalization-QR decomposition method is a procedure to diagonalize the whole matrix. It produces exact eigenvalues and eigenvectors within the numerical error of the computer. It utilizes the complex symmetric banded structure of the stochastic Liouville matrix, but it does not take advantage of the sparsity of the matrix as do the Lanczos or CG algorithms. This is our method of choice when $R \lesssim 10^{-6}$ s^{-1} for nitroxides, although it unfortunately leads to substantial computation times.

The projections of the eigenvectors of a matrix onto a given vector may be obtained by keeping track of the effect that the Jacobi rotations which annihilate the off-diagonal matrix elements have on that vector. In the simulation of cw spectrum where one needs only the eigenvalues and the weighting factors, which are the projections of the eigenvectors on the starting vector, it is only necessary to monitor the effect of the Jacobi rotations on the starting vector.[31] Using the (1,0,...,0) vector instead of the starting vector projects out the first element of each of the eigenvectors. Thus *all* the eigenvectors are obtained by monitoring the Jacobi rotations on the unit matrix of dimension n.[32] This makes the eigenvector calculation substantially more computation-intensive than the eigenvalue calculation. The CPU time is roughly proportional to $n^2 n_b$, where n_b is the bandwidth of the matrix. For $n=122$, $n_b=34$, the eigenvalue and eigenvector calculation took 11 s, whereas the eigenvalue and weighting factor calculations took 2.5 s on an IBM RS6000/355 workstation in double precision complex arithmetic. For $n=372$, $n_b=53$, the corresponding CPU times are 311 and 23 s. This example shows that the dimension of the matrix is critical for computational efficiency. Practical application of this method would be quite difficult for matrix dimensions over 3000 (for eigenvalue calculations) or 2000 (for the full analysis) even using a supercomputer. A scheme to minimize the dimension of the matrix is described in Sec. III D. But for such large matrices we prefer to use the RA to obtain just the eigenvalues, coupled with the CG algorithm for projecting the eigenvectors.

Spectral simulation based on calculation of the cross-correlation function in Eq. (29) is particularly useful for the Rutishauser algorithm. As shown in Eq. (29), simulating 2D-ELDOR spectra requires the eigenvalues of the diagonal subspace and the $O_0^{\mathrm{tr}}|u_{\pm 1}(t)\rangle$ vector, which is the projection of the diagonal eigenvectors on the multiple starting vectors of the diagonal subspace defined in Eq. (28). This can be easily achieved by monitoring the effect of the Jacobi rotations on the multiple starting vectors of the diagonal subspace. If the number of starting vectors $O_0^{\mathrm{tr}}|u_{\pm 1}(t)\rangle$ to be used (i.e., the number of distinct values of t_1 and t_2 in the experiment) is smaller than the dimension of the diagonal subspace, the correlation function approach is more efficient. The total number of distinct values of t_1 and t_2 necessary to represent a 2D-ELDOR spectrum does not depend on the dimension of the matrix n, and we find 128 points along t_1 and t_2 axes are sufficient. The relative advantage of the correlation function approach over the explicit calculation of the eigenvectors (when utilizing the RA) becomes more significant as the matrix dimension increases and/or as the number of points along t_1 and t_2 axes decreases. Note that the eigenvectors of the off-diagonal space are still needed to determine the $|u_{\pm 1}(t)\rangle$ starting vectors [cf. Eq. (29)] and to simulate SECSY or S_{c-} COSY spectra [cf. Eq. (13)]. But the diagonal space is the more demanding.

D. Minimum truncation scheme (MTS) and basis set pruning

The dimension of the matrix is very important for computational efficiency, but it is necessary to obtain a minimum basis set that represents the spectrum without distortion. It is crucial for the Rutishauser method since it does not take full advantage of the sparsity of the matrix, but it is also important for the Lanczos-based methods.

A general and objective way of determining a minimum set of basis vectors necessary to represent the accurate cw spectrum has been studied using the CG method by Vasavada *et al.*, which is called the field-swept CG method.[12] It utilizes the fact that each element in the solution vector of the CG method is proportional to the importance of the corresponding basis vector in representing the cw ESR spectrum at the sweep position. It was found that by repeating the conjugate gradient calculation for 10–20 sweep positions one can safely determine the importance of each basis vector, and that it is sufficient to keep only basis vectors which have a projection greater than 0.03 onto the normalized solution vector for at least one sweep position in order to obtain an accurate cw ESR spectrum. We refer to this analysis whereby we remove the unimportant basis vectors as "pruning" the basis set and to the resultant basis set as the minimum truncation scheme (MTS).[10] Thus, the MTS just described is referred to as one based on a 3% pruning tolerance. As the additional inhomogeneous broadening contribution increases, the number of important basis vectors for a given pruning tolerance decreases, since the fine details of the spectrum would be blurred by large inhomogeneous broadening anyway.

The same principle can also be applied to the simulation of the COSY or SECSY spectrum, which involves the off-diagonal space. Rather than specifying the range of the indices of the basis vectors or using case-dependent truncation rules,[12] it is desirable to construct the pruned basis set by explicitly examining the contribution of each basis vector at all the field positions. We find that repeating the field-swept CG calculation at 50 sweep positions with a pruning tolerance of 3% and 0.5 G of inhomogeneous broadening width is a conservative way of obtaining the pruned basis set for calculating an absolute-value 2D-ESR spectrum (i.e., showing the magnitude of the complex signal intensity).

Obtaining the MTS for the diagonal space becomes more complicated than for the off-diagonal space, due to the problem of multiple starting vectors (although a convenient choice would be the linear combination noted in Sec. III A). Repeating field-swept CG for multiple starting vectors would be costly, but we found an alternative way. Once we obtain the pruned basis set for the off-diagonal space, we can con-

TABLE I. MTS and the effect of pruning as a function of motional rates.[a]

R (s^{-1})	L_e[b]	L_o[b]	K[b]	M[b]	n_{np}[c]	n_1[d]	n_0[d]	n_i[e]	n_b[e]	n_{ev}[f]	t_{vec} (s)[g]	t_{val} (s)[h]
10^4	66	27	22	2	2313	912	1552	5955	66	499	2737	163
10^5	34	17	14	2	798	372	570	2454	53	219	311	23
10^6	16	9	6	2	204	122	188	708	34	76	11	2.5
10^7	6	3	2	2	42	34	50	134	22	24	0.7	
10^8	2	0	2	1	13	9	11	13	7	3		

[a]Parameters used for obtaining the pruning indices: B_0=3200 G, g_{xx}=2.0092, g_{yy}=2.0059, g_{zz}=2.0021, $A_{xx}=A_{yy}$=4.9, A_{zz}=34.2. Additional linewidth of 0.5 G was added. Field-swept CG was performed at 51 field positions with ±45 G range. The tolerance for terminating the CG iteration was 10^{-4}. A pruning tolerance of 3% was used.

[b]L_e, L_o, K, M are the maximum number of the corresponding indices found in the pruned basis set. The subscript e, and o means even and odd L values, respectively.

[c]n_{np}: dimension of the off-diagonal basis set when all the basis vectors within the specified L_e, L_o, K, M range are included.

[d]n_1, n_0: dimensions of the off-diagonal and the diagonal subspaces, respectively after pruning.

[e]n_i: the number of nonzero elements in the off-diagonal subspace of the stochastic Liouville matrix; n_b: the bandwidth of the matrix in the off-diagonal subspace with the pruned basis set.

[f]n_{ev}; number of eigenvectors that have significant projection on the starting vector in the off-diagonal subspace.

[g]t_{vec}; CPU time for calculating eigenvalues and eigenvectors. An IBM RS6000 was used.

[h]t_{val}; CPU time for just calculating eigenvalues and weighting factors using the RA. For $R \gtrsim 10^6$ s^{-1} the LA leads to significantly reduced t_{val} and t_{vec}.

struct the corresponding basis set for the diagonal space using the pulse propagator in Eq. (26). The dimension of the diagonal space is approximately twice that of the off-diagonal space since each basis vector in the off-diagonal space is transformed to two basis vectors in the diagonal space (except for $p^I = M = 0$). A careful numerical test shows that this diagonal basis set represents all the important eigenmodes without distortion. This approach has three distinct advantages: (i) One field-swept CG calculation in the off-diagonal space generates the basis set for both off-diagonal and diagonal spaces. (ii) The eigenvectors in the diagonal space can be transformed into the off-diagonal space using the pulse propagator in Eq. (27) to reduce the storage space by half. (iii) There is a simple correspondence between the basis sets in the diagonal and off-diagonal spaces.

The effect of explicit pruning in various cases is summarized in Table I in terms of the dimension of the matrix, the number of nonzero elements, and CPU time (for the RA). Obtaining the MTS is a fast procedure since (i) it uses the CG algorithm which utilizes the sparsity of the matrix; (ii) it depends on the weighting factors which are obtained without calculating the eigenvectors explicitly; and (iii) this dependence on weighting factors makes it insensitive to the spurious effects arising from roundoff error.[10]

When the motional rate is relatively fast ($R \gtrsim 10^6$ s^{-1}), the spectral simulations are reasonably fast, especially when the LA is utilized, so that one can fit the experimental spectra with an automated NLLS procedure. Since NLLS fitting is an iterative process that requires many spectral simulations, it is absolutely essential to work with the pruned basis set. However, NLLS fitting of multidimensional spectra presents little additional computational burden, since 2D spectra such as the $S_{c\pm}$ COSY, and 3D data sets such as a 2D-ELDOR spectrum measured at different mixing times may be simulated using a single set of eigenvalues and eigenvectors, and one needs to diagonalize the stochastic Liouville matrix only once to fit all spectra. Fitting multiple spectra also enhances the resolution and sensitivity to the motional and structural parameters obtained by NLLS minimization.

IV. RESULTS AND DISCUSSION

The applicability of 2D techniques depends on the homogeneous and inhomogeneous linewidths of the spectrum. The overall linewidth, which is the sum of the homogeneous linewidth T_2^{-1} and the inhomogeneous linewidth $T_2'^{-1}$, is represented by the characteristic decay constant T_2^*; i.e., $T_2^{*-1} = T_2^{-1} + T_2'^{-1}$. Another important decay constant is the T_1 relaxation that governs the decay of magnetization in the diagonal subspace. In actuality, the decay rates (i.e., the relaxation constants) must reflect the complicated nature of the spin and motional dynamics. Therefore lineshape analyses and relaxation studies are required to provide important insights into the details of the dynamics.

We first examine the dependence of the T_2 type of relaxation on the motional rate. The SECSY experiment yields the homogeneous linewidths (i.e., T_2^{-1}) across the spectrum. The homogeneous linewidths are merely the real parts of the eigenvalues in the off-diagonal space with $p^S = -1$, which are shown in Fig. 2(a) as a function of the motional rate for a typical ^{14}N nitroxide. Brownian motion is assumed in the calculation, and the rotational correlation time τ_R is $1/(6R)$, where R represents the isotropic rotational rate. In the fast motional regime ($R \gtrsim 10^8$ s^{-1}), one needs only three eigenvalues, which represent the three hyperfine lines. As the motion slows down below the rate of $R \sim 10^7$ s^{-1}, the number of significant eigenmodes (n_{ev} in Table I) increases. The eigenvalues of four typical slowly decaying modes (i.e., narrow lines) are shown in Fig. 2(a) to illustrate the dependence on the motional rate, even though there exist many other important eigenmodes. Note that the log–log plot produces a linear dependence in this motional regime, and it can be modeled as $T_2^{-1} \propto \tau_R^{-c}$. Linear fits of the plot yield values for the exponent c ranging from 0.55 to 0.70.[17]

Typical decay rates of the eigenvectors in the diagonal subspace are shown in Fig. 2(b). To examine the contribution of the rotational motion to the relaxation, the role of the rotationally independent electron spin flip rate W_e in the diagonal subspace is suppressed and the rotationally indepen-

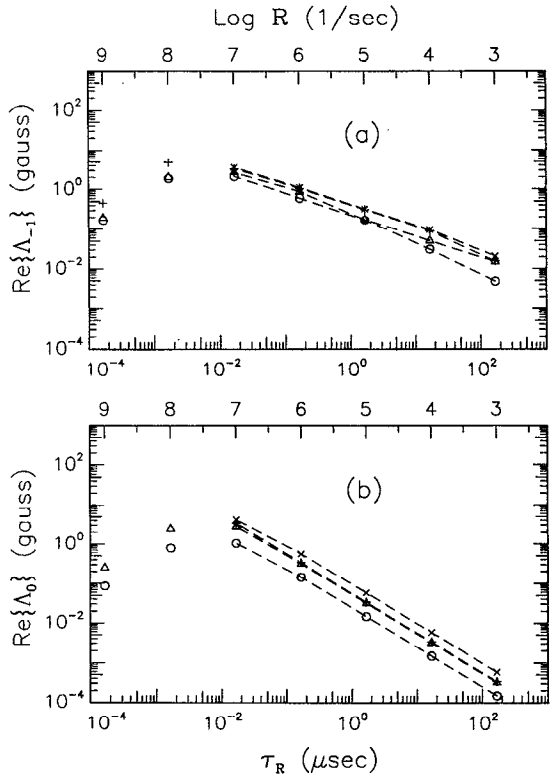

FIG. 2. Linewidths as a function of the motional rate for Brownian motion. (a) $\mathrm{Re}\{\Lambda_{-1}\}$ vs R (or τ_R), (b) $\mathrm{Re}\{\Lambda_0\}$ vs R (or τ_R). The value of $2W_e$ is fixed at $10^{-5}\ \tau_R^{-1}$ to minimize the role of $2W_e$ in the relaxation. In the fast motional regime, all the important eigenmodes (except $2W_e$) in the diagonal subspace are shown. In the motional range slower than $R=10^7\ \mathrm{s}^{-1}$, only four of the important eigenmodes corresponding to slow decay rates are shown (except $2W_e$). The parameters used for the simulation are: B_0=3200 G, g_{xx},g_{yy}=2.0075, g_{zz}=2.0021, $A_{xx}=A_{yy}$=4.9 G, A_{zz}=34.0 G. The pruned basis sets obtained with a 1% tolerance and inhomogeneous broadening of 0.5 G are used for all motional rates. Axial tensors are assumed to reduce the dimension of the matrix.

dent nuclear spin flip rate W_n is set to zero. The general trend is similar to that of the off-diagonal subspace, and the number of significant eigenvectors are comparable to the off-diagonal case. Four typical slowly relaxing eigenmodes are shown in the plot for motional rates of $R<10^7\ \mathrm{s}^{-1}$, and an equivalent analysis to that for the off-diagonal space yields an exponent of 1. Note that there is much less scatter in the slope in the diagonal subspace than in the off-diagonal subspace. Schwartz[18] previously found that these modes have a simple correspondence to the fast-motional eigenmodes, viz. they correspond approximately to relaxation rates of $2W_e$ [not shown in Fig. 2(b)], $2W_e + 3W_n^{\mathrm{rot}}$, and $2W_e+\tau_R^{-1}$, where W_n^{rot} is the rotationally induced nuclear spin–flip rate discussed in Sec. IV D below. Our present results are in agreement with such an assignment, although we find more than one mode with nearly the same relaxation rates.

With a current spectrometer deadtime of ~50 ns and time resolution of 1 ns in our laboratory, it is difficult to observe a signal whose T_2 (for echoes) or T_2^* (for FIDs) is shorter than ~15–30 ns. Since the homogeneous linewidth itself is large in the motional range of $\sim 10^6 < R < \sim 10^7\ \mathrm{s}^{-1}$ for nitroxides, most of the examples given below will concentrate on the two motional ranges where the FID or the echo signal can be acquired experimentally—viz. the relatively fast motional regime and the very slow motional regime.

A. The S_{c+} vs S_{c-} signal

Simulation of the relatively fast motional regime is a fairly easy problem for the following reasons. (i) The dimension of the matrix becomes small since only small L values are needed in the basis set as indicated in Table I. (ii) One can ignore the contribution of the nuclear Zeeman term for ^{14}N or ^{15}N when the motion is sufficiently fast to average out the nuclear modulation.[17] Under these conditions, one needs to diagonalize only one of the off-diagonal spaces because the relations $O_{-1}=O_1^*$, $\Lambda_{-1}=\Lambda_1^*$, are valid. (iii) One can use virtually any diagonalization routine since the eigenvalues are well separated. The Lanczos algorithm is just as reliable as the Rutishauser algorithm in this motional range and is significantly faster.

Two mirror image coherence transfer pathways with respect to t_1 are responsible for the COSY or the 2D-ELDOR signals as indicated in Fig. 1. Since the matrix Λ_{-1} (eigenvalues of the $p^S=-1$ subspace) is complex conjugate to the matrix Λ_1 (eigenvalues of the $p^S=1$ subspace) in the absence of the nuclear Zeeman term, the cancellation of the imaginary part in the S_{c-} signal leads to the formation of an echo at $t_1=t_2$, whereas the S_{c+} signal has no echolike property. If the nuclear Zeeman contribution is not negligible, as in the very slow motional regime, the imperfect cancellation results in modulation of the echo envelope [i.e., electron spin echo envelope modulation (ESEEM)].

The differences between the S_{c+} signal and the S_{c-} signal in Eqs. (13) and (15) depend on the motional rate, since slow motions lead to inhomogeneous broadening, and on other sources of inhomogeneous broadening; the latter are not explicitly included in the stochastic Liouville equation. Assuming the inhomogeneous broadening to be given by a Gaussian distribution, the two signals can be written as[33]

$$S_{c\pm}^{\mathrm{GIB}}=S_{c\pm}\ e^{-2\pi^2\Delta_G^2(t_1\pm t_2)^2}, \tag{33}$$

where $S_{c\pm}^{\mathrm{GIB}}$ is the broadened signal and Δ_G is the Gaussian inhomogeneous broadening parameter in frequency units. Unresolved superhyperfine interactions with protons is a typical source of Gaussian inhomogeneous broadening in nitroxide spectra.

To examine the difference between the S_{c+} signal and the S_{c-} signal due to the motional rate, it is convenient to rewrite the COSY signal given in Eq. (13) in the absence of the nuclear Zeeman term as

$$\begin{aligned} S_{c+}^{\mathrm{COSY}}(t_1,t_2)&=\sum_i w_i^2 e^{-\lambda_i(t_1+t_2)},\\ S_{c-}^{\mathrm{COSY}}(t_1,t_2)&=\sum_{i,j} w_i e^{-\lambda_i t_2}(O^{\mathrm{tr}}O^*)_{ij}e^{-\lambda_j^* t_1}w_j^*, \end{aligned} \tag{34}$$

where w_i is the projection of the ith eigenvector on the starting vector. O and λ_i denote the matrix of eigenvectors and

the ith eigenvalue of the $p^S=-1$ off-diagonal subspace. Note that w_i^2 corresponds to the weighting factor of the ith eigenvector.

In the fast-motional regime ($R>10^8$ s^{-1}), the eigenvectors of the off-diagonal space become real, so $O^{tr}O^*=O^{tr}O=1$ and $w_i^* = w_i$. Then the only difference between the S_{c+} and S_{c-} signals in Eq. (34) is that the S_{c+} signal evolves with λ_i and the S_{c-} signal evolves with λ_i^* during the t_1 period, which means the magnetization is rotating in opposite directions. If the isotropic part of the (Gaussian) inhomogeneous broadening is negligible (the anisotropic part, if present, is averaged out by the rapid rotational motion), then the refocusing property of the S_{c-} signal does not matter, and the S_{c-} signal becomes the mirror image of the S_{c+} signal along the axis $\omega_1=0$. Then the sum of the two signals is proportional to $e^{i\omega t_1} + e^{-i\omega t_1} = 2\cos(\omega t_1)$, which is a pure absorption with respect to t_1. Therefore, if both coherence transfer pathways are kept in the phase cycling, one can obtain the pure absorption spectrum by cosine Fourier transform.[23]

As the motion slows down below the rate of $R\sim10^8$ s^{-1}, averaging of hyperfine and g tensors is incomplete for a typical ^{14}N nitroxide at X band, and this is a source of inhomogeneous broadening. Also the magnetic tensors appear in the imaginary part of the stochastic Liouville matrix, and their incomplete averaging causes the eigenvectors to deviate from being purely real. Fig. 3 shows the decay of the real part of the S_{c+} and S_{c-} signals in the time domain for the case of $R=10^8$ s^{-1} and no Gaussian inhomogeneous broadening. The S_{c+} and S_{c-} signals are no longer equivalent. The complex nature of the eigenvectors introduces a phase change in the S_{c-} signal [i.e., $O^{tr}O^*$ in Eq. (34) is a complex matrix] and allows for mixing (or "beating") of different eigenmodes in S_{c-} [cf. Eq. (34)]. Therefore the S_{c-} signal loses its coherence in phase whereas the S_{c+} signal does not. This loss of phase coherence appears as the interference pattern near the $t_1=t_2$ axis in the S_{c-} signal. The S_{c+} signal propagates like a coherent wave, maintaining its phase coherence throughout the decay in t_1 and t_2. The overall decay rates of the two signals are similar if the motion is faster than $R\sim10^6$ s^{-1}. But for $R\lesssim10^6$ s^{-1} the S_{c+} signal does decay significantly faster than the S_{c-} signal in a fashion more typical of the effect of ordinary inhomogeneous broadening, as a result of the nearly continuous eigenvalue spectrum (cf. Sec. III A).

The inhomogeneous broadening due to incomplete averaging of the proton superhyperfine tensor also becomes significant as the motion slows. Eq. (33) implies that the intensities of the two signals are affected in different ways due to Gaussian inhomogeneous broadening. Whereas both signals are multiplied by the same exponentially decaying function along the $t_1=0$ or $t_2=0$ axes, only the S_{c+} signal is multiplied by the decaying function along the $t_1=t_2$ axis. Thus, the S_{c+} signal decays with T_2^* and the S_{c-} signal decays with T_2 along the $t_1=t_2$ axis because the inhomogeneous broadening is completely canceled in the S_{c-} signal. Therefore the S_{c-} signal will be more intense than the S_{c+} signal after the finite deadtime. The case where there is Gaussian inhomogeneous broadening, but the motion is fast enough to average the magnetic tensors, is illustrated in Fig. 4 and it shows this feature. Also, the line shape of the S_{c-} signal in the frequency domain tends to be elongated along the diagonal through the autopeaks, whereas the S_{c+} signal keeps its symmetric shape.

As the motion slows sufficiently, the inhomogeneous broadening will dominate the decay ($T_2 \gg T_2^*$), and it is impossible to observe the S_{c+} signal after the finite deadtime, since it decays with T_2^*. However since the homogeneous linewidth decreases as the motion approaches the rigid limit [cf. Fig. 2(a)], one is able to detect the S_{c-} signal in the form of an echo provided the T_2 decay is not too fast compared to the spectrometer deadtime.

Due to the phase change resulting from the complex eigenvectors, and the intensity change from the inhomogeneous broadening and finite deadtime, it is not possible to obtain a pure absorption spectrum simply by combining two experiments from the mirror image coherence transfer pathways. Furthermore, to avoid the need for phase corrections arising from experimental limitations, the absolute-value (or magnitude) spectrum is typically utilized.[4–7] Therefore the absolute-value spectrum will be displayed throughout most of this paper.

We show in Fig. 5 an experimental realization of these various effects taken from Lee *et al.*[6] for the case of 2D-ELDOR in a complex fluid where there is substantial inhomogeneous broadening resulting from unresolved proton superhyperfine interactions and from another source discussed in Sec. IV C below. Note first of all the refocusing property of the S_{c-} signal along the $t_1=t_2$ diagonal, whereas this is not the case for the S_{c+} signal [cf. Fig. 5(b) vs Fig. 5(a)]. Note that the S_{c+} signal, which is more affected by inhomogeneous broadening, decays more rapidly during the finite deadtime, causing it to be weaker than the S_{c-} signal after FT [cf. Fig. 5(c) vs Fig. 5(d)]. In this ELDOR case we see that the ratio of the crosspeak heights relative to the autopeak heights is smaller for the S_{c-} signal compared to the S_{c+} signal. This is because only the autopeaks in the S_{c-} signal can experience an exact cancellation of the inhomogeneous broadening along $t_1=t_2$, so they are sharper than the S_{c-} crosspeaks. These experimental spectra have been fitted to the present theory, and the relevant dynamic and ordering parameters found appear in the caption to Fig. 5.

B. Homogeneous linewidth from the S_{c-} COSY

Standard two pulse sequences ($\pi/2-\pi$ or $\pi/2-\pi/2$) can be used to obtain the homogeneous linewidth when $T_2 \gg T_2^*$. The SECSY experiment with a hard pulse has the advantage over the conventional Hahn echo method with a soft pulse in that the linewidths across the spectrum are obtained from a single experiment (multiplex advantage). One gets interference from the FID signal if T_2 and T_2^* are not much different as in the incipient slow motional regime. One obvious remedy for the problem has been to apply an external field gradient to force the FID signal to decay faster (i.e., T_2^* gets shorter). Whereas the external inhomogeneous field

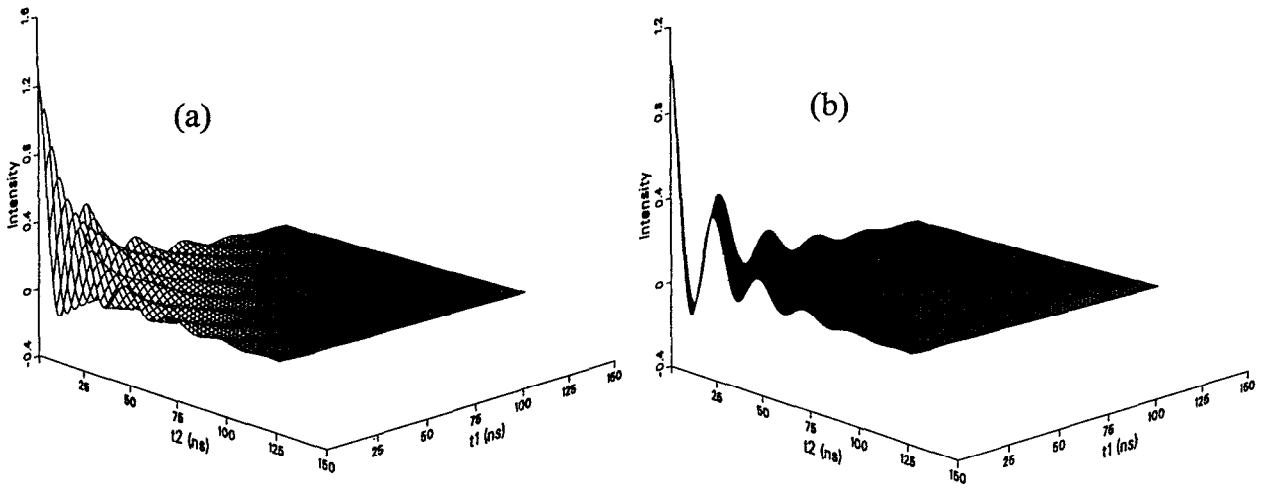

FIG. 3. The effect of incomplete averaging of hyperfine and g tensors. The COSY spectra in the time domain are shown for (a) the S_{c-} signal and (b) the S_{c+} signal. The parameters used for the simulation are: B_0=3200 G, g_{xx}, g_{yy}, g_{zz}=2.0092, 2.0059, 2.0021, $A_{xx}=A_{yy}$=4.9 G, A_{zz}=34.2 G, $R_\perp=1.0\times10^8$ s^{-1}, $R_\parallel=1.0\times10^8$ s^{-1}, $L_{\max}$=4. No Gaussian inhomogeneous broadening is added (i.e., Δ_G=0 G).

does not affect the Hahn echo method, it broadens the SECSY spectrum along the ω_2 direction, resulting in the loss of resolution.

An alternative way is to realize that the S_{c-} signal is the term responsible for the echo. Even though the S_{c-} COSY signal looks like a FID signal in the incipient slow motional regime, it is really the same signal that would generate an echo at $t_1=t_2$. This can be seen in Fig. 4(a). Following the $t_1=0$ axis, the signal looks like a FID. Following the $t_1=200$ ns axis, the signal looks like a perfect echo. This implies that the S_{c-} COSY signal can be transformed into a SECSY-like format to generate the homogeneous linewidth across the spectrum without applying an external magnetic field.

From Eq. (13), the S_{c-} COSY signal can be written as

$$S_{c-}^{\mathrm{COSY}}(t_1,t_2)\propto\sum_{l,j} c_{lj}e^{-\lambda_l^{(1)}t_1}e^{-\lambda_j^{(-1)}t_2}, \tag{35}$$

where $\lambda_l^{(1)}$ and $\lambda_j^{(-1)}$ are the eigenvalues of the $p^S=1$ and $p^S=-1$ subspaces, respectively. The coefficients c_{lj} are given by

$$c_{lj}=\sum_{i,k,m}(v_{-1})_i(O_{-1})_{ij}(O_{-1})_{kj}(O_1)_{kl}(O_1)_{ml}(v_1)_m. \tag{36}$$

The SECSY signal, ignoring the contribution of the nuclear Zeeman term, is obtained by replacing t_2 with t_1+t_2. Using the complex conjugate relations $O_{-1}=O_1^*$, $\Lambda_{-1}=\Lambda_1^*$ (i.e., $\lambda_j^{(-1)}=\lambda_j^{(1)*}$), and dropping the super- and subscripts denoting the p^S values, the SECSY signal is

$$S_{c-}^{\mathrm{SECSY}}(t_1,t_2)\propto\sum_{l,j} c_{lj}e^{-(\lambda_l+\lambda_j^*)t_1}e^{-\lambda_j^*t_2},$$
$$c_{lj}=\sum_{i,k,m} v_iO_{ij}^*O_{kj}^*O_{kl}O_{ml}v_m. \tag{37}$$

The autopeaks appear when $c_{lj}=\delta_{lj}$, and they can be written as

$$\text{autopeaks of } S_{c-}^{\mathrm{SECSY}}(t_1,t_2)\propto\sum_j e^{-(\lambda_j+\lambda_j^*)t_1}e^{-\lambda_j^*t_2}$$
$$=\sum_j e^{-2\,\mathrm{Re}(\lambda_j)t_1}e^{-\lambda_j^*t_2}. \tag{38}$$

This shows that the linewidth appears along the ω_1 direction and the cw-equivalent spectrum appears along the ω_2 direction in the SECSY spectrum. The inhomogeneous linewidth broadens the spectrum only along the ω_2 direction, but one still recovers the homogeneous linewidth in the ω_1 direction due to cancellation of the imaginary part.

Now we will show how one can achieve the same result by dividing the S_{c-} COSY spectrum into two parts and performing a shearing transformation. Defining $t_2=t_1+t_2'$ for the region $t_2>t_1$ and following the same algebra as for SECSY [cf. Eq. (38)], Eq. (35) can be rewritten as

$$\text{autopeaks of } S_{c-}^{\mathrm{COSY}}(t_1,t_2')$$
$$\propto\sum_j e^{-(\lambda_j+\lambda_j^*)t_1}e^{-\lambda_j^*t_2'} \quad \text{for } t_2>t_1 \tag{39}$$

which is exactly the same as for SECSY. For the region $t_2<t_1$, defining $t_1=t_1'+t_2$ gives

$$\text{autopeaks of } S_{c-}^{\mathrm{COSY}}(t_1',t_2)$$
$$\propto\sum_j e^{-\lambda_jt_1'}e^{-(\lambda_j+\lambda_j^*)t_2} \quad \text{for } t_2<t_1. \tag{40}$$

The information content in Eq. (40) is the same as that in Eq. (39), although the roles of t_1 and t_2 are interchanged. These transformations of the axis show that one can still retrieve the homogeneous linewidth from the COSY spectrum by eliminating the S_{c+} signal by dual quadrature data

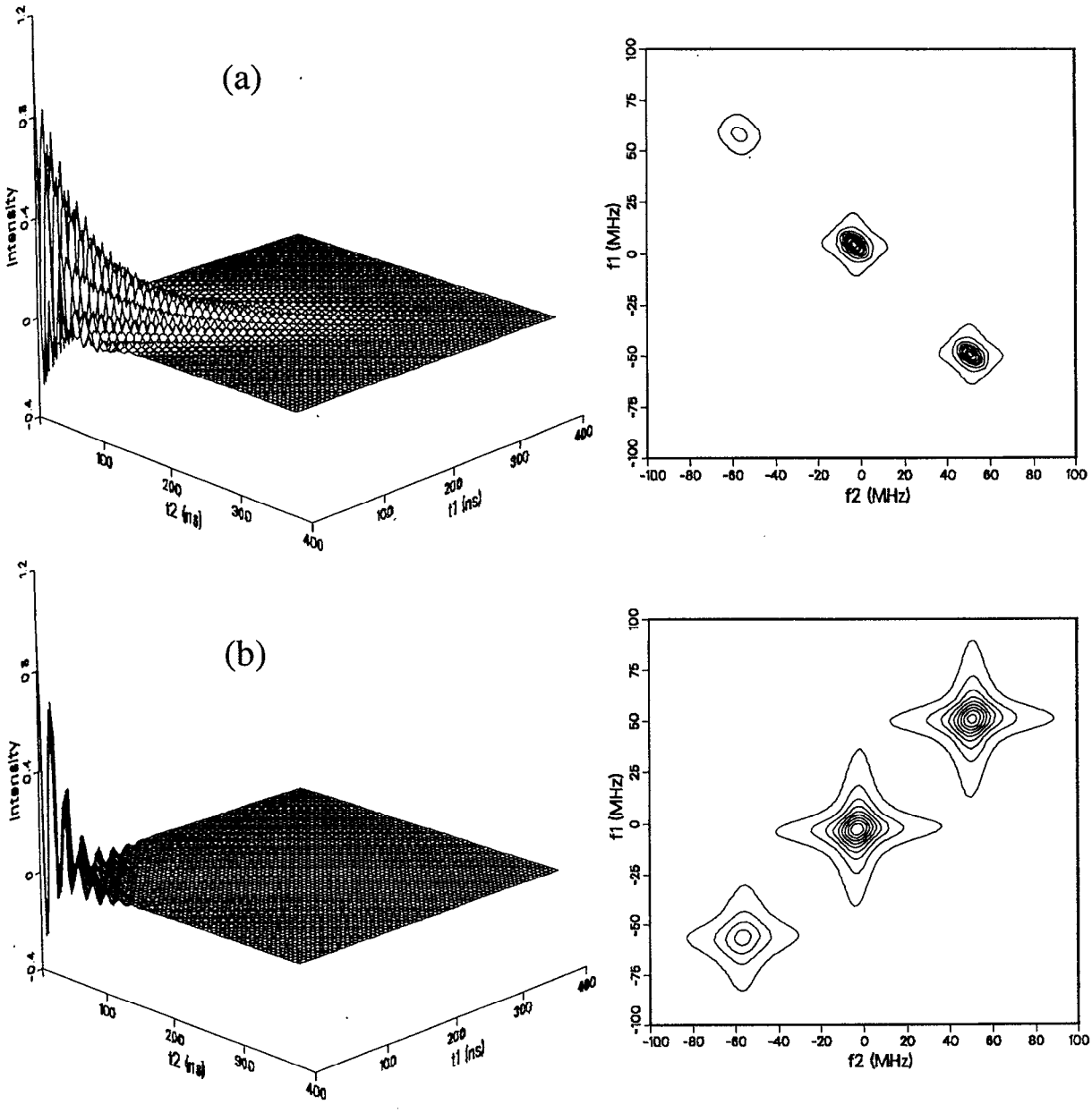

FIG. 4. The effect of Gaussian inhomogeneous broadening. The COSY spectrum in time (left-hand side) and frequency (right-hand side) domains for (a) the S_{c-} signal and (b) the S_{c+} signal. The same parameters listed in Fig. 3 are used except $R_\perp = 4.0\times10^8\ s^{-1}$, $R_\parallel = 8.0\times10^8\ s^{-1}$, $\Delta_G = 1$ G. Absolute-value spectra are shown for the spectra in the frequency domain.

collection.[25] Therefore it is not necessary to quench the FID by applying a field gradient, which would decrease the resolution in the ω_2 direction, to obtain the homogeneous linewidth across the spectrum. Note that the COSY-transformed-into-SECSY format has better sensitivity than SECSY itself, since it is based on the whole FID collection, and not just on the decaying half of the echo. Even in the case where only the echo signal is observed, one can still collect the entire echo and use the transformations. This would increase the sensitivity by $\sqrt{2}$ since one has both the refocusing and the dephasing parts of the echo.

C. Inhomogeneous broadening (microscopic order macroscopic disorder effect)

The difference between the S_{c+} and S_{c-} signal mostly originates from inhomogeneous broadening as indicated earlier. Most sources of inhomogeneous broadening distinct from those due to slow motions can be approximated as Gaussian or Lorentzian. An important class of exceptions appears in samples with microscopic molecular ordering such as liquid crystalline, model membrane, and polymer samples. These long-chain molecules can often be aligned

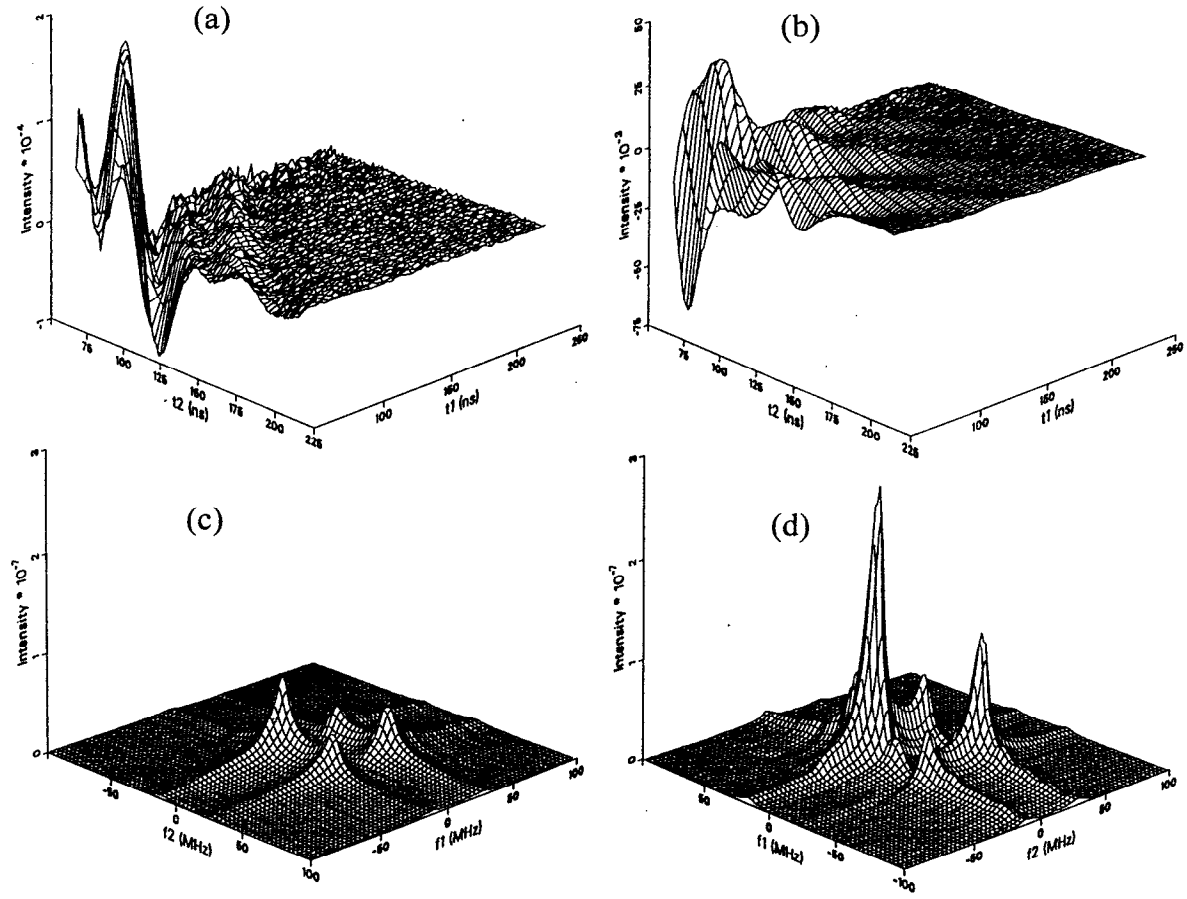

FIG. 5. Experimental 2D-ELDOR spectra for a mixing time of $T=87$ ns from the spin-labeled lipid 12-PC [1-palmitoyl-2-(12-doxyl stearoyl phosphatidylcholine] in a phospholipid membrane vesicle of POPC [1-palmitoyl-2oleoyl-sn-glycerophosphatidylcholine] at 55 °C. (a) the S_{c+} signal and (b) the S_{c-} signal in the time domain. (c) the S_{c+} signal and (d) the S_{c-} signal in frequency domain. Note the difference in scale in (a) and (b). The scales in (c) and (d) are the same. The parameters estimated from the nonlinear least-squares fitting procedure are: $R_\perp=4.6\times10^8\ s^{-1}$, $R_\parallel=1.4\times10^9\ s^{-1}$, $\epsilon_0^2=1.0$, $\epsilon_2^2=-0.4$, $\Delta_G=0.4$ G. The deadtimes for t_1 and t_2 are 50 and 67 ns, respectively (Ref. 6). The magnetic parameters used are: $B_0=3200$ G, $g_{xx}, g_{yy}, g_{zz}=2.0092$, 2.0059, 2.0021, $A_{xx}=A_{yy}=4.9$ G, $A_{zz}=34.2$ G.

along a specific direction (i.e., the director) resulting in macroscopic order. The molecular reorientational dynamics in the presence of a tendency to order is modeled by a (symmetrized) rotational diffusion superoperator with a restoring potential of the form

$$U(\Omega)=-k_BT\sum_{L=2,4}\{\epsilon_0^L\mathscr{D}_{00}^L(\Omega)+\epsilon_2^L[\mathscr{D}_{02}^L(\Omega)+\mathscr{D}_{0-2}^L(\Omega)]\}, \tag{41}$$

where $\Omega=(\alpha,\beta,\gamma)$ represents a set of Euler angles describing the orientation of the diffusion tensor with respect to the director axis. The director tilt angle ψ is defined as the angle between the director axis and the magnetic field.

In an effort to explain the ESR spectrum of lipid dispersion samples which lack any macroscopic order, the microscopic order macroscopic disorder (MOMD) model was introduced by Meirovitch *et al.*[34] It regards the dispersion sample as a collection of fragments whose director axes are distributed isotropically in space (macroscopic disorder). Within a given fragment, the molecules are well aligned along the director axis (microscopic order). Then the spectrum from the dispersion sample can be regarded as the superposition of the spectrum from all fragments, which can be written as

$$S_{c\pm}^{\mathrm{MOMD}}=\int S_{c\pm}(\psi)\sin\psi\, d\psi \tag{42}$$

where $S_{c\pm}(\psi)$ is the ESR spectrum with the director angle ψ. The effect of the MOMD model on the cw ESR spectrum is also illustrated in Meirovitch *et al.* It has recently been applied in the analysis of cw ESR spectra of spin labeled lipids in di-palmitoyl-phosphatidyl-choline/gramicidin A.[35] The orientation dependence of the real and imaginary parts of the eigenvalues for a typical nitroxide attached along the chain is illustrated in Fig. 6 as a function of ψ. The resulting MOMD spectrum is shown in Fig. 6(c) in an absolute-value plot. The outer peaks show more broadening than the central peak, since they show more variation in the imaginary part of the eigenvalues. As the orienting potential increases [large epsi-

lons in Eq. (41)], the line shape becomes more asymmetric, and one can observe a hump in the outer lines, while the central line becomes slightly asymmetric. All these characteristics of the MOMD model observed in the cw ESR spectrum also apply to the 2D spectrum.

Figure 7 shows typical S_{c+} and S_{c-} 2D-ELDOR spectra based on the MOMD model. The corresponding cw spectrum is shown in Fig. 6(c). Whereas the line shape along the autopeaks in the S_{c-} signal (negative diagonal axis) resembles the cw spectrum, the line shape of the autopeaks in the S_{c+} signal looks quite different, showing only the two extrema of the frequency distribution due to the MOMD model for each hyperfine line. [The extrema can be clearly seen in the outer hyperfine lines where the frequency variation due to the MOMD model is large, cf. Fig. 6(b).] This seems to be due to a combination of the absolute-value display along both dimensions used to avoid the phase problem associated with the two-dimensional Fourier transformation, and the superposition of the eigenmodes resulting from the distribution of the director axis in the MOMD model. Note that the experimental example of Fig. 5 corresponds to this MOMD case.

The same kind of superposition occurs in simulations we have performed of rigid limit (i.e., powder) COSY spectra. Since the resonance frequency depends on the orientation of the micro crystal, the orientational average in a powder spectrum can be viewed as the integral in Eq. (42). The powder spectrum is not much different from the spectrum at a very slow motional rate (near the rigid limit). We simulated the S_{c+} and S_{c-} COSY spectra at a near rigid limit motional rate, and confirmed that they have similar lineshapes to those in the MOMD spectra in Fig. 7. Note that the S_{c+} signal in this motional regime decays too fast to be detected in real experiments.

The crosspeaks with $\Delta m_I = \pm 1$ in the 2D-ELDOR spectra shown in Fig. 7 exhibit the opposite trend to that noted above for the autopeaks. The S_{c+} signal shows a smooth shape, and the S_{c-} signal shows extrema. It should be pointed out that these fine details may not be easily observed in an experiment. The ordering potential should be large to have an appreciable MOMD effect. This makes the S_{c+} signal decay much faster than the S_{c-} signal, resulting in a much weaker signal not as likely to be detectable after the deadtime. Also, the additional inhomogeneous broadening (Gaussian or Lorentzian) smears out the fine details of the spectrum.

In Fig. 8 we show an experimental 2D-ELDOR spectrum for the case of MOMD with a large ordering potential from the study of Crepeau *et al.*[7] Only the S_{c-} signal is detectable after the finite deadtime. Note that the peak shapes reflect the MOMD effect; i.e., compare with Fig. 7(b). However in Fig. 8 one has a different principal axis of alignment than in Fig. 7, leading to some differences in detail of the autopeak shapes, and the experimental spectrum of Fig. 8 has incipient slow motional effects as well. We list in the figure caption the relevant dynamic and ordering parameters found by a NLLS fit of the theory to this spectrum.

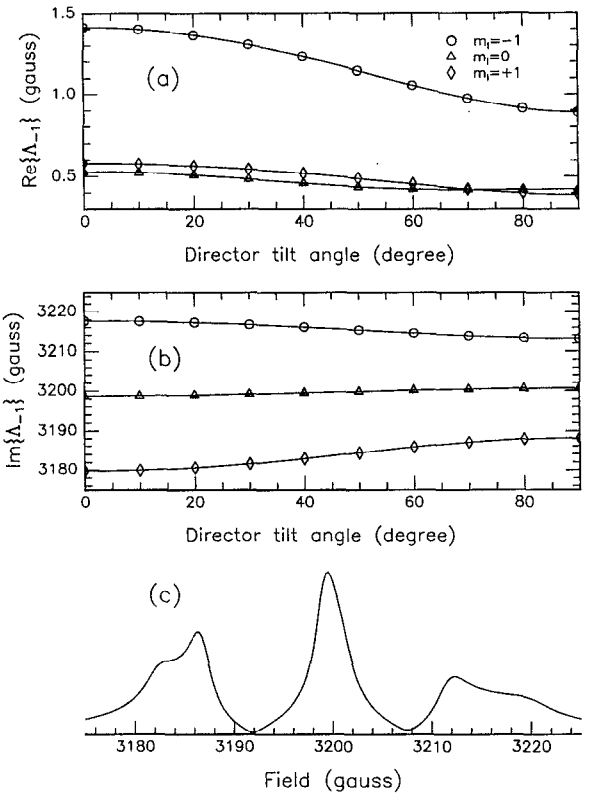

FIG. 6. The effect of MOMD: (a) $\mathrm{Re}\{\Lambda_{-1}\}$ vs director tilt angle (b) $\mathrm{Im}\{\Lambda_{-1}\}$ vs director tilt angle (c) cw ESR spectrum based on the MOMD model averaged over 20 director tilt angles. The absolute-value field-swept spectrum is shown for comparison to the 2D spectra in Fig. 7, which are obtained with frequency sweep. The parameters used for the simulation are: B_0=3200 G, g_{xx}, g_{yy}, g_{zz}=2.0092, 2.0059, 2.0021, $A_{xx}=A_{yy}$=4.9 G, A_{zz}=34.2 G, $R_\perp=4.0\times10^8\ \mathrm{s}^{-1}$, $R_\parallel=8.0\times10^8\ \mathrm{s}^{-1}$, β_D=0°, $L_{\max}$=4. A potential coefficient of ϵ_0^2=1.0 ($S\sim0.22$) is used to provide microscopic ordering for the MOMD effect, and additional Gaussian inhomogeneous broadening of 0.5 G is included (Δ_G=0.5 G).

D. Ultraslow motional regime (near rigid limit)

The simulation of the near rigid limit is a challenging problem, since the dimension of the matrix becomes larger as the motion slows down. This makes the RA very inefficient especially for eigenvector calculations. For a matrix with n=912 and n_b=66 at a motional rate of $R=10^4\ \mathrm{s}^{-1}$, the full eigenvector calculation took about 35 min on a IBM RS6000/355 workstation. It is difficult to use Lanczos-based algorithms, since the test for spurious and duplicate eigenvalues is not very reliable because the eigenvalues are not well separated (cf. Sec. III A). We chose to use the RA with a minimized basis set to avoid any complications. Possible improvement of performance is expected by using the RA based on calculating the cross-correlation function rather than the eigenvectors (cf. Sec. III C). It should be emphasized that the dimension of the matrix should be minimized by selecting only the necessary basis vectors using the full pruning scheme described in Sec. III D. Only the S_{c-} signal is available in the form of an echo in this motional regime due to the inhomogeneous broadening, and the spectra will be shown in SECSY format (i.e., autopeak along f_1=0). Fig-

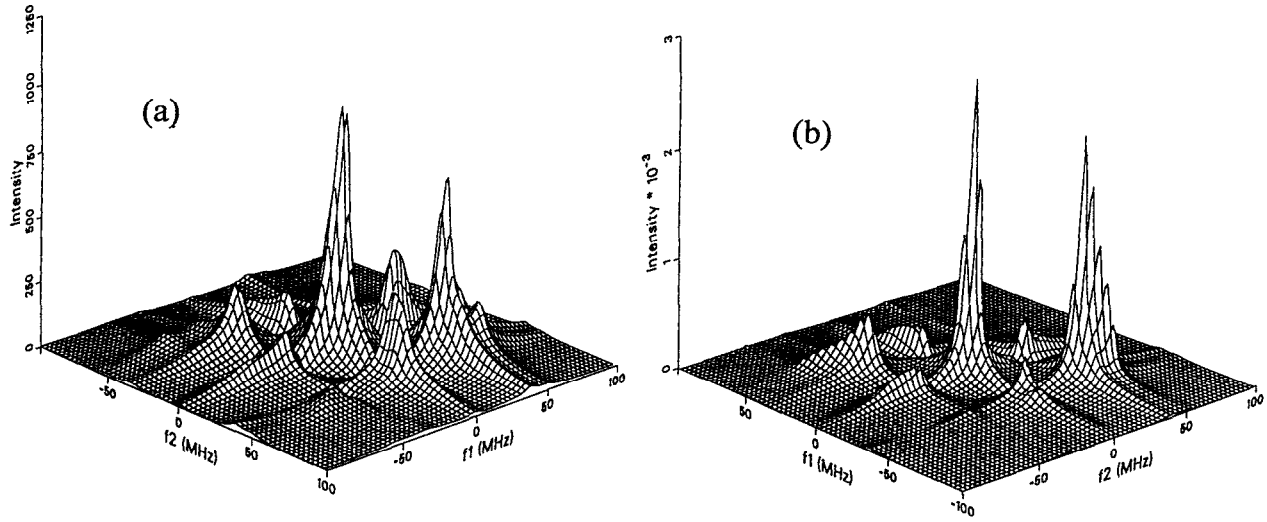

FIG. 7. 2D-ELDOR spectra with the MOMD model for (a) the S_{c+} signal and (b) the S_{c-} signal. The same parameters listed in Fig. 6 are used. Additional parameters for the 2D simulation are: initial $t_1, t_2 = 0$ ns, steps in t_1 and t_2 (i.e., Δt_1 and Δt_2) are 5 ns, with 128 t_1, t_2 values, mixing time $T = 100$ ns. Absolute-value plots are shown. Notice the difference in scale in S_{c+} and S_{c-}.

ure 9 shows the SECSY and 2D-ELDOR spectra with $R = 10^4$ s^{-1} for a typical nitroxide. Note that the crosspeaks between the two autopeaks at $(f_1, f_2) = (0, f_a)$ and $(0, f_b)$ appear at $(f_a - f_b, f_a)$ and $(f_b - f_a, f_b)$ in the SECSY format.

The apparent linewidths of the autopeaks in 2D-ELDOR spectra increase as the mixing time increases. This is due to the development of the crosspeaks arising from the slow rotational motion ("motional crosspeaks").[5] The development of these motional crosspeaks appears as line broadening since the eigenmodes represent a virtual continuum of the orientations in the near rigid limit; i.e., one is observing "rotational jumps" from each orientation to all other orientations by the Brownian rotation. The cw ESR spectra for motional rates slower than $R = 10^6$ s^{-1} are essentially in the rigid limit, e.g., there is no difference between the cw spectra from $R = 10^5$ and 10^4 s^{-1}, but this is not the case for the 2D spectra.

The apparent linewidth broadening due to the development of motional crosspeaks provides a method of measuring the rotational correlation time in the motional regime where the cw ESR spectrum is in the rigid limit and the lineshape analysis is insensitive to the motional rate. The following procedure illustrates how one can approximately obtain the rotational correlation time from the experimental spectrum. Slices along $f_2 = 0$ MHz are extracted from the absolute-value spectra in Fig. 9, and are shown in Fig. 10. The broadening of the $f_1 > 0 (f_1 < 0)$ region represents the development of the crosspeaks between the original autopeak (i.e., $f_2 = 0$ MHz) and the autopeaks at $f_2 < 0 (f_2 > 0)$ MHz. An attempt to fit the spectra was made using a NLLS fit to the absolute-value spectrum using a single Lorentzian line as

$$y = c[T_2^{-2} + 4\pi^2 (f - f_0)^2]^{-1/2} + (\text{baseline correction}) \tag{43}$$

with $f_0 = 0$. (This ignores details of the shapes, most evident at long mixing times, T, which reflect the intensities of the autopeaks at the different values of $f - f_0$.) The nominal linewidth T_2 for each mixing time is found to satisfy the following:

$$\Delta T_2^{-1}(T_m) \equiv T_2^{-1}(T_m) - T_2^{-1}(0) = \frac{T_m}{a \tau_R}, \tag{44}$$

where $T_2^{-1}(0)$ is the linewidth of the 2D-ELDOR spectrum with zero mixing time, i.e., the SECSY spectrum. τ_R denotes the rotational correlation time, and it is $1/(6R)$ for the isotropic Brownian motional model. The linewidths from five mixing times $T_m = 0,3,5,10,20$ μs were analyzed by linear least squares to produce $a = 1.0 \times 10^{-2}$ μs for $R = 10^4$ s^{-1}. The same procedure was repeated for $R = 10^5$ s^{-1} where $T_m = 0,100,200,500,1000$ ns were used, resulting in $a = 1.2 \times 10^{-2}$ μs. The constant a is thus found to be independent of the motional rate as expected and to be $\sim 1.1 \times 10^{-2}$ μs. (The same result was obtained from slices taken along $f_2 = 78$ MHz.) Then one can obtain τ_R from Eq. (44) by measuring the linewidths of the SECSY and 2D-ELDOR spectra.

The dependence of a on the hyperfine tensor component A_{zz} was also examined at a motional rate of $R = 10^5$ s^{-1}. The value of a was 2.2×10^{-2} μs for $A_{zz} = 27$ G, 1.1×10^{-2} μs for $A_{zz} = 34.2$ G, and 0.7×10^{-2} μs for $A_{zz} = 40$ G, keeping other magnetic parameters constant. It showed a monotonic decrease with A_{zz} within this range. This result is sensible since a smaller value of a implies a faster development of the rotational crosspeaks, which is expected for a larger hyperfine tensor. [In fact, we find that a^{-1} plotted vs A_{zz} yields a good linear fit with a slope of $(5.41 \pm 0.35) \times 10^6$ s^{-1} G^{-1} and an intercept of $(-96 \pm 12) \times 10^6$ s^{-1}].

In Fig. 11 we show slices along $f_2=0$ MHz from experimental 2D-ELDOR spectra taken in the very slow motional regime[5] for a range of mixing times of 3–30 μs. They were analyzed in an identical fashion to the simulated spectra. We obtained $(a\tau_R)^{-1}=0.19$ $(\mu s)^{-2}$ corresponding to a $\tau_R\approx 480$ μs when the theoretical estimate of a from Fig. 10 is used. This illustrates that 2D-ELDOR is indeed sensitive to very slow motions approaching the millisecond time scale, and that estimates of τ_R are easily obtained in the manner described.

In addition to the motional crosspeaks, there are the regular $\Delta m_I=\pm 1$ crosspeaks observed in Fig. 9 as we noted above. They arise from nuclear spin–flips induced by rotational modulation of the hyperfine tensor, as was the case for the faster motions. It is possible to estimate their rate of growth in the case of simple isotropic rotational diffusion (i.e., the growth of these cross-peak volumes compared to the autopeak volumes), by analogy to the fast-motional case of 2D-ELDOR.[2] A simple perturbation theory analysis based on the SLE will lead to a decoupling of the forbidden ESR transition basis elements $(p^S=0,p^I\neq 0)$ from the allowed transitions $(p^S=\pm 1,p^I=0)$, and the nuclear magnetic resonance (NMR) transitions $(p^S=0,p^I\neq 0)$ from the populations $(p^S=0,p^I=0)$. It was shown previously[36,37] that this leads to a simple expression for the rotationally induced nuclear spin flip rate (for ^{14}N):

$$W_n^{(\mathrm{rot})}=\frac{D^2}{5}\,\frac{\tau_R}{1+\tilde{b}_2^2\tau_R^2}\,, \tag{45}$$

where

$$\tau_R=1/(6R),\quad D=-\frac{3}{2}\left(\frac{1}{\sqrt{6}}\right)|\gamma_e|(A_\parallel-a_N),$$

$$\tilde{b}_2=-\frac{1}{2}\,|\gamma_e|\left[a_N+\frac{1}{2}\,(A_\parallel-a_N)\right],$$

where it is assumed $A_{xx}=A_{yy}=A_\perp$ with $a_N=\mathrm{Tr}(\mathbf{A})$ and the nuclear Zeeman term is much smaller than a_N. [For ^{15}N the value of $W_n^{(\mathrm{rot})}$ is half that given by Eq. (45).] This result is essentially the fast-motional result, but a previous numerical analysis by Schwartz[18] has shown that this is a useful approximation even for slow motions, and our present results are consistent with it. For slow motions, Eq. (45) goes asymptotically as $(D^2/5)\tilde{b}_2^{-2}\tau_R^{-1}$. The actual experiments[5] have, however, shown that it is necessary to include a rotationally independent contribution to W_n to explain the more rapid decay of the autopeak intensities (due to the growth of the $\Delta m_I=\pm 1$ crosspeaks) than is consistent with the τ_R obtained from the motional crosspeaks. Such a contribution is included in the general theoretical expressions given in Appendix B.

We have also considered the effect of anisotropic rotational rates on the very slow motional 2D-ELDOR spectra. We illustrate with a large anisotropy of $R_\parallel/R_\perp=100$ for two different orientations of the principal diffusion axes with respect to the magnetic tensor principal axes. When $R_\parallel$ refers to the magnetic z axis we have only a modest change in spectral shapes versus the isotropic case [compare Figs. 12(a) and 12(b) with Figs. 9(a) and 9(c)]. The largest differences appear in the $T=0$ (i.e., SECSY) spectra which just show the autopeaks. When $R_\parallel$ refers to the magnetic x axis, the line shape changes are more dramatic [cf. Figs. 12(c) and 12(d)], and the behavior is also significantly different from that of isotropic spectra calculated for $R_\parallel=R_\perp=10^6$ s^{-1} (not shown). These sample spectra illustrate the potential of 2D-ELDOR spectral simulations for resolving motional anisotropy in the very slow motional regime.

The problem of large dimensional matrices in simulating the ^{14}N nitroxide spectrum in the near rigid limit can be partially alleviated by using ^{15}N isotopic labeling, which reduces the size of the matrices by a factor of 4/9. The SECSY and the 2D-ELDOR spectra for a ^{15}N nitroxide are shown in Fig. 13. The same g-tensor values were used as in the ^{14}N nitroxide spectrum in Fig. 9, and the hyperfine tensor values were scaled by the ratio of the nuclear gyromagnetic ratios of ^{15}N vs ^{14}N. The increase in the apparent linewidth is qualitatively the same as for a ^{14}N nitroxide, and the equivalent analysis at motional rates of $R=10^4$ and 10^5 s^{-1} yielded $a=3.3\times 10^{-3}$ μs.

Another important question is how one can distinguish between restricted [i.e., highly ordered (HO)] but fast motion and true slow motion (SM) given the spectral similarities for these two cases noted in the previous subsection. In both cases, the range of rotational angle sampled by the molecule within a short time is quite limited. We can model the restricted but fast motion by specifying a large restoring potential and a fast rotational rate. Fig. 14 shows the SECSY and the 2D-ELDOR spectra based on the MOMD model with a potential coefficient $\epsilon_0^2=10.0$, and $\Delta_G=0.1$ G for ^{15}N. Note that the appearance of the SECSY spectrum is quite similar to the SECSY spectrum near the rigid limit without any restoring potential shown in Fig. 13(a). This implies that it will be difficult to distinguish the two cases in the presence of inhomogeneous broadening with the cw ESR spectra, which is equivalent to the autopeaks in SECSY. (The SECSY resolution can, however, be enhanced by obtaining the pure absorption rather than the magnitude spectrum as discussed in Sec. IV F) However, the resulting 2D-ELDOR spectra are significantly different as can be seen in Figs. 13 and Fig. 14. Near the rigid limit without any restoring potential, the slow rotational motion can still change the orientation of the molecule into any angle. Therefore the crosspeaks develop in a continuous fashion as in Fig. 13. In the MOMD model, however, the range of motion is restricted by the strong restoring potential, and each different orientation angle corresponds to a different local domain. The fast rotational motion within each local domain dominates and leads primarily to the development of the standard $\Delta m_I=\pm 1$ crosspeaks compared to the rotational crosspeaks. (However, rotational crosspeaks can result from the very slow reorientation of the domain structure[7] which has not as yet been included in our MOMD model.) Therefore the crosspeaks from the MOMD model appear more distinct in Fig. 14 than in Fig. 13.

The rate of crosspeak development depends, of course, on the motional rate. Whereas the spectra near the rigid limit show slow development of "rotational" crosspeaks (e.g., 5 μs in Fig. 13), the crosspeaks in the restricted but fast mo-

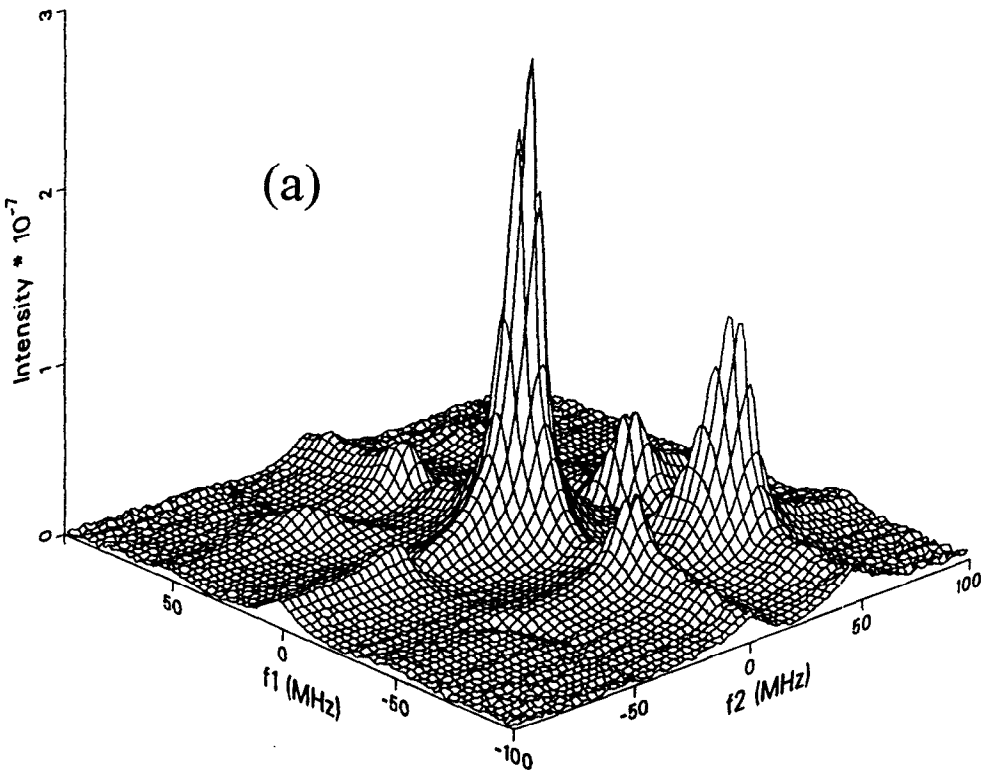

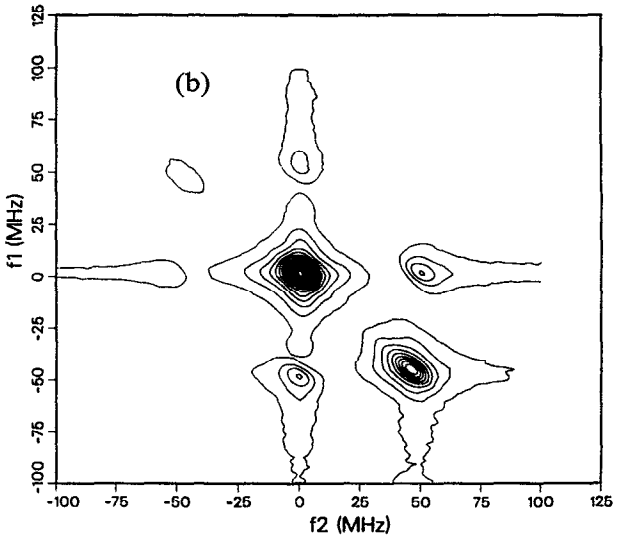

FIG. 8. The experimental 2D-ELDOR spectra from cholestane spin label (CSL) in phospholipid membrane vesicles of POPC at 50 °C. (a) Surface plot and (b) contour plot of the S_{c-} signal are shown for $T=400$ ns. The parameters estimated from the nonlinear least-squares fitting procedure are: $R_\perp=3.9\times10^7\ s^{-1}$, $R_\parallel=1.0\times10^9\ s^{-1}$, $\epsilon_0^2=5.0$, $\epsilon_2^2=1.6$, $\epsilon_0^4=-0.5$, $\Delta_G=1.3$ G. The deadtimes for t_1 and t_2 are 50 and 67 ns, respectively (Ref. 7). The magnetic parameters used are: $B_0=3200$ G, $g_{xx}, g_{yy}, g_{zz}=2.0081$, 2.0061, 2.0024, $A_{xx}, A_{yy}, A_{zz}=5.6$, 5.3, 33.8 G. Also, $\beta_D=90°$ and $\gamma_D=75°$. The S_{c+} signal decays away during the deadtime due to the large inhomogeneous broadening and MOMD effect. Note that the autopeaks of the S_{c-} signal appear along the negative-diagonal axis, $f_1=-f_2$.

tional case fully develop within a short period (e.g., 1 μs in Fig. 14). If any slow reorientation of the local domain were present in the MOMD model, the crosspeaks would develop in a continuous fashion over a long mixing period in addition to fast and distinct growth.[6] In favorable cases where the two time scales are well separated, 2D-ELDOR may be able to distinguish the two processes.

E. Nuclear modulation

Nuclear modulation of the electron-spin echo has been utilized mainly to study nuclei that are weakly coupled to the electron spin by dipolar interaction, thereby yielding structural information. So far, most ESEEM experiments are performed in the solid state and the effect of molecular rotational motion has hardly been studied.[38] However, it is clear from the results of Patyal *et al.*[4,5] that nuclear modulation is an important component in 2D-ESR spectra even in the presence of residual motion. We present model simulations of nuclear modulation phenomena for SM and for rotational motion restricted by a restoring potential (HO).

Simulation of the nuclear modulation requires the pseudosecular dipolar and the nuclear Zeeman terms in the

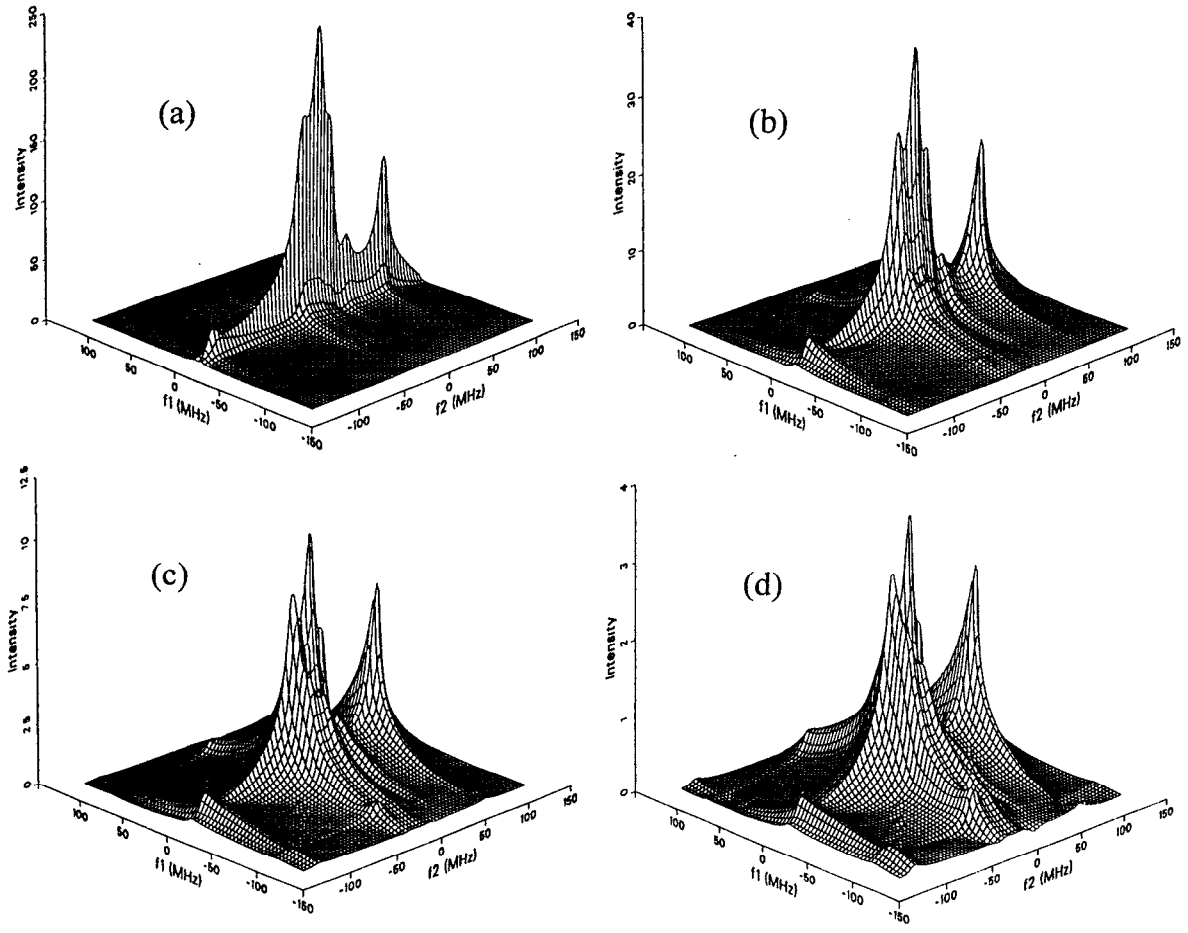

FIG. 9. 2D-echo-ELDOR spectra near the rigid limit ($R=10^4$ s^{-1}) for mixing times of (a) $T=0$ μs, i.e., the SECSY spectrum, (b) $T=3$ μs, (c) $T=10$ μs, (d) $T=20$ μs. The simulation parameters are: $R=10^4$ s^{-1}, g_{xx},g_{yy},g_{zz}=2.0096, 2.0063, 2.0022, A_{xx},A_{yy},A_{zz}=6.5, 4.5, 33.4 G, Δ_G=1.0 G, $L^e_{\max}$=56, $L^o_{\max}$=27, $K_{\max}$=18, $M_{\max}$=2, and B_0=3200 G. A pruned basis set was obtained with a 3% tolerance. Initial t_1,t_2=0 ns, steps in t_1 and t_2 (i.e., Δt_1 and Δt_2) are 4 ns, and 128 t_1,t_2 values are used for the 2D simulation.

Hamiltonian. Since the nuclear Zeeman terms appear as off-diagonal with respect to the index j^M, the stochastic Liouville matrix is no longer block diagonal with respect to j^M. Therefore it is necessary to keep those basis vectors with $j^M=-1$, which causes a considerably larger basis set. The presence of both symmetric ($j^M=1$) and antisymmetric ($j^M=-1$) basis vectors causes the eigenvalues and the eigenvectors of the $p^S=\pm 1$ subspaces to occur in pairs, where the eigenvalues of each subspace are complex conjugates of the other, and the eigenvectors have more complicated internal relationships we discuss next.

The nuclear Zeeman term in the spin Hamiltonian does not change sign with respect to the index p^S [cf. Eq. (A10)], whereas the g- and hyperfine-tensor terms in the Hamiltonian do change sign [cf. Eqs. (A9) and (A10)]. Therefore, the two off-diagonal subspaces seem to require separate diagonalizations in general. However, a more careful examination shows that the eigenvalues and the weighting factors of the two off-diagonal subspaces still remains as complex conjugates of each other (i.e., $\Lambda_{-1}=\Lambda_1^*$). The eigenvectors differ only in the sign of their components corresponding to the basis vectors with $j^M=-1$ after complex conjugation. Therefore once the eigenvectors for the $p^S=1$ subspace are obtained, the prescription for obtaining the eigenvectors of the $p^S=-1$ subspace is to take the complex conjugate of the eigenvectors of the $p^S=1$ subspace, and multiply each element by the j^M value of the corresponding basis vector. We do recover the property $O_{-1}=O_1^*$ in the absence of the nuclear Zeeman term, since the basis vectors with $j^M=-1$ are no longer necessary.

Motional averaging of the nuclear modulation patterns was illustrated by Schwartz *et al.* in terms of echo envelope decay[17,38] With the second dimension experimentally available, a better way of examining the nuclear modulation effect is the SECSY, or echo-ELDOR experiment.[33] We show a SECSY simulation near the rigid limit ($R=4.63\times10^3$ s^{-1}) in Fig. 15(a), which shows the nuclear modulation pattern displayed along the f_1 direction. The hyperfine-tensor elements and the nuclear gyromagnetic ratio are appropriate for a proton located at ~3.8 Å from the unpaired electron. The modulation of the echo envelope gradually decreases as the motional rate increases, and disappears when the rate of the

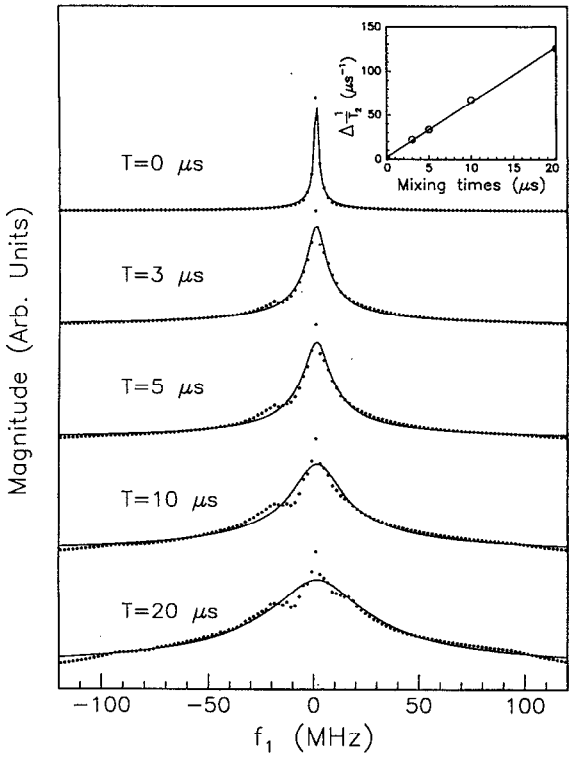

FIG. 10. ω_2=0 MHz slices of 2D-ELDOR spectra in Fig. 9. The solid lines show the best fit to the absolute value of the single Lorentzian as shown in Eq. (43). The resulting linewidth plot is shown in the inset. The slope of the linear fit is 6.2 μs^{-2}.

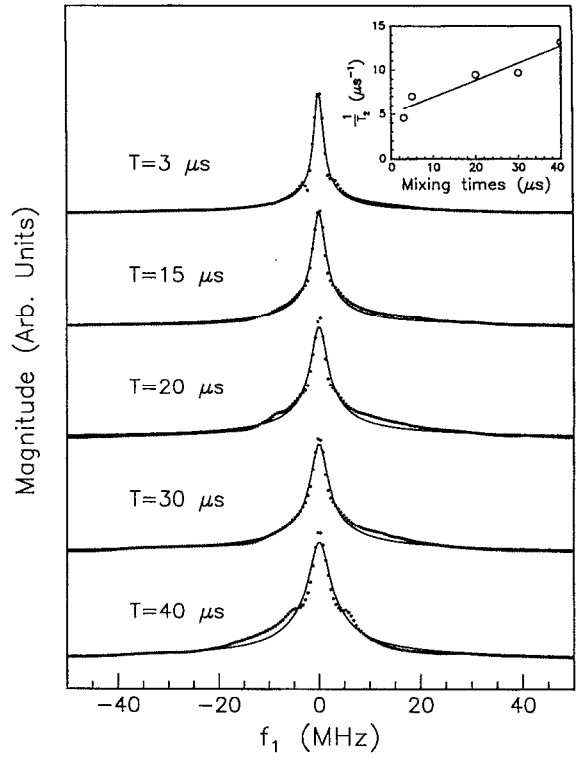

FIG. 11. ω_2=0 MHz slices of 2D-ELDOR spectra from perdeuterated tempone in 85% glycerol–15% H_2O at −73 °C (Ref. 5). The resulting linewidth plot vs T is shown in the inset. The slope of the linear fit is 0.19 μs^{-2}.

rotational motion is faster than $R=10^7$ s^{-1} (i.e., $\tau_R \lesssim 17$ ns).[17] Another way of recovering the modulation pattern is by restricting the motional range by adding a strong restoring potential. As the restoring potential increases, the spectrum becomes more single-crystal-like, and the nuclear modulation pattern becomes more prominent (unless the director axis coincides with one of the hyperfine tensor axes[33]). The SECSY spectrum from a dispersion sample may be again approximated by the MOMD model, and results from averaging over 20 director tilt angles are shown in Fig. 15(b). Even though the autopeaks in Figs. 15(a) and 15(b) are significantly different, it may be difficult to distinguish the two cases from the shape of the autopeaks in the presence of a large inhomogeneous broadening. However, additional modulation peaks in Fig. 15(b) may still be used to distinguish between restricted but fast motion (HO) and SM.

F. Normalized contour plots and the pure absorption spectrum

Normalized contour plots were introduced as a way of examining the field-swept 2D-ESE spectrum by Millhauser and Freed.[20,39] For every field position, the slice along the f_1 direction is normalized so that the amplitude at f_1=0 MHz is unity. This can be regarded essentially as the homogeneous linewidth (T_2^{-1}) plot across the spectrum, and it is found to be very sensitive to the motional dynamics and models. For example, these authors were able to observe a significant variation of the linewidth across the slow motional spectrum from tempone in 85% glycerol/water, which could be explained by Brownian diffusion, but not by jump diffusion.

As we already discussed, the cw ESR spectral simulations are found to converge with a pruning tolerance of just 3%, since the inhomogeneous contributions to the linewidth reduce the resolution. However, the homogeneous linewidths predicted near the rigid limit are found to increase as one tightens the pruning tolerance versus 3% (i.e., by including more basis vectors), and the linewidth reaches approximately 95% of the limiting value with a pruning tolerance of 0.03%. Since a normalized contour plot of the field-swept 2D ESE directly monitors the homogeneous linewidth, its simulation requires much tighter tolerance than the cw ESR simulation. Vasavada *et al.* proposed the use of 0.03% as a conservative tolerance.[12]

The two dimensional version of field-swept ESE is a SECSY experiment. The use of hard pulses in SECSY enables one to obtain the homogeneous linewidth across the spectrum in significantly less time. However, it is not trivial to obtain a pure absorption spectrum[4] because one must correct the phase errors due to effects of finite dead-time and finite irradiating fields.[2,40,41] In an absolute-value display of the SECSY spectrum, the interference from the dispersive components of neighboring dynamic spin packets reduces the resolution, and the normalized contour plot does not show as much variation of linewidth across the spectrum as the field-swept ESE. This problem is exacerbated near the

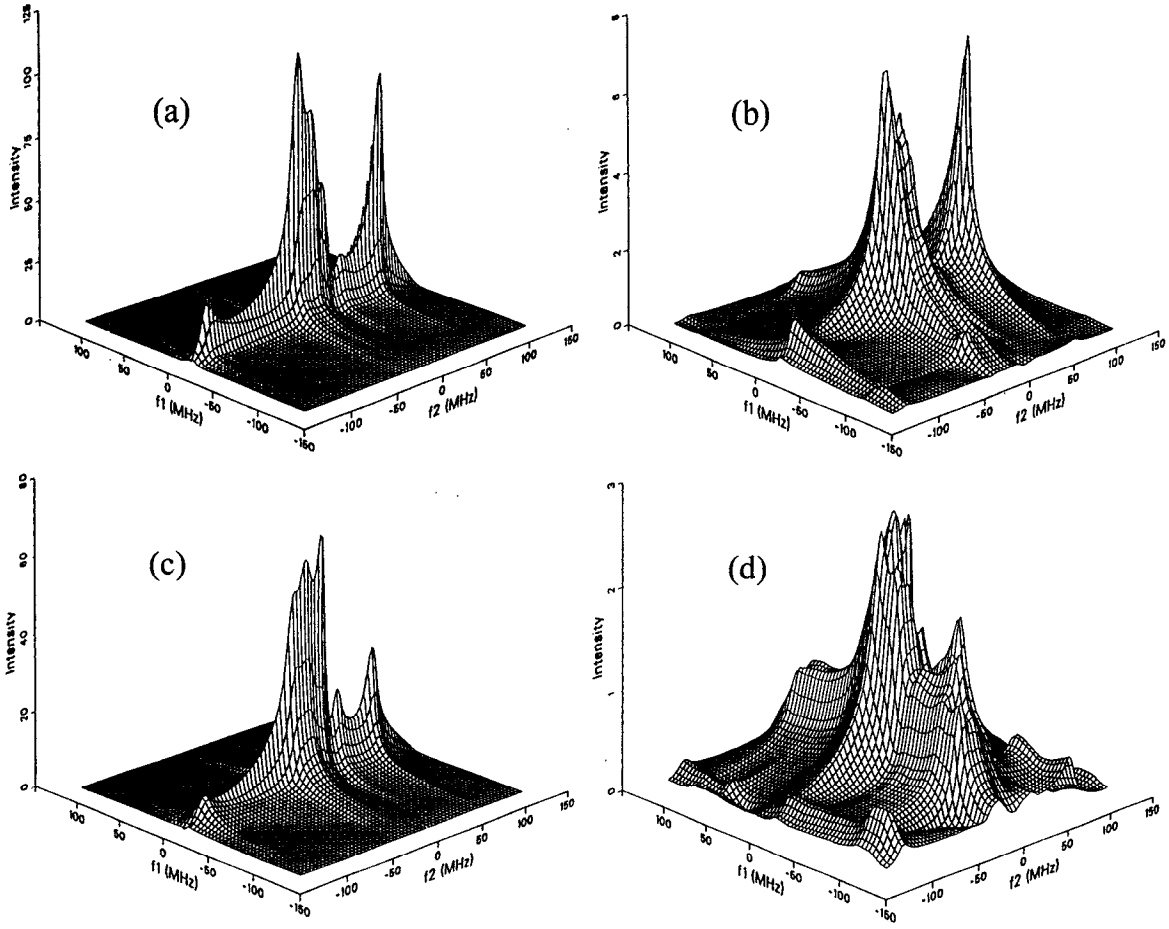

FIG. 12. The effect of anisotropic rotational rates: 2D-echo-ELDOR spectra simulated with $R_x=R_y=10^4\ s^{-1}$, $R_z=10^6\ s^{-1}$ are shown for mixing times of (a) $T=0\ \mu s$, (b) $T=10\ \mu s$. The case where $R_y=R_z=10^4\ s^{-1}$, $R_x=10^6\ s^{-1}$ is shown in the simulations of (c) $T=0\ \mu s$ (d) $T=10\ \mu s$. Other parameters are the same as in Fig. 9.

rigid limit where the resonance frequencies of the dynamic spin packets are a continuum. Since the absolute-value plot of the SECSY spectrum provides reduced sensitivity to the homogeneous linewidth, its simulation is usually satisfied with a pruning tolerance of 3%. Field-swept ESE does not have the problem of mixed phase, since it yields a pure absorption inherently along the swept field, and one dimensional Fourier transform is used to measure the linewidth at each field position.

A numerical experiment that demonstrates the loss of resolution in the absolute-value plot is shown in Fig. 16. Note the significant difference in the pure absorption spectrum and the absolute-value spectrum. It demonstrates the importance of incorporating phase corrections[4,41] to recover the pure absorption spectra in 2D-FT studies of very slow motions.

V. SUMMARY AND CONCLUSIONS

A theory of 2D-FT ESR that covers the entire range of motion in a liquid has been developed based on the stochastic Liouville approach. Relaxation processes such as the rotational motion of the molecule and Heisenberg exchange are explicitly included in the stochastic Liouville matrix. Detailed expressions for two and three pulse sequences were derived from the coherence transfer pathway analysis of the multiple pulse sequence. The theory is general enough to simulate various 2D-FT ESR spectra from any one electron and one nucleus system in the strong pulse and high field limit.

The symmetry properties of the stochastic Liouville matrix were examined in detail in order to reduce the dimension of the stochastic Liouville matrix. The effect of the pulse propagator on the symmetrized basis set was found to preserve the symmetries of the density matrix existing before the pulse.

Key computational aspects involved in the simulation of the 2D-FT ESR spectra were discussed. Special algorithms to deal with large sparse matrices were described in terms of the eigenvector calculation. Also, a general scheme of minimizing the dimension of the basis set was provided.

The differences in the signals from the two mirror image coherence transfer pathways were explained in terms of the

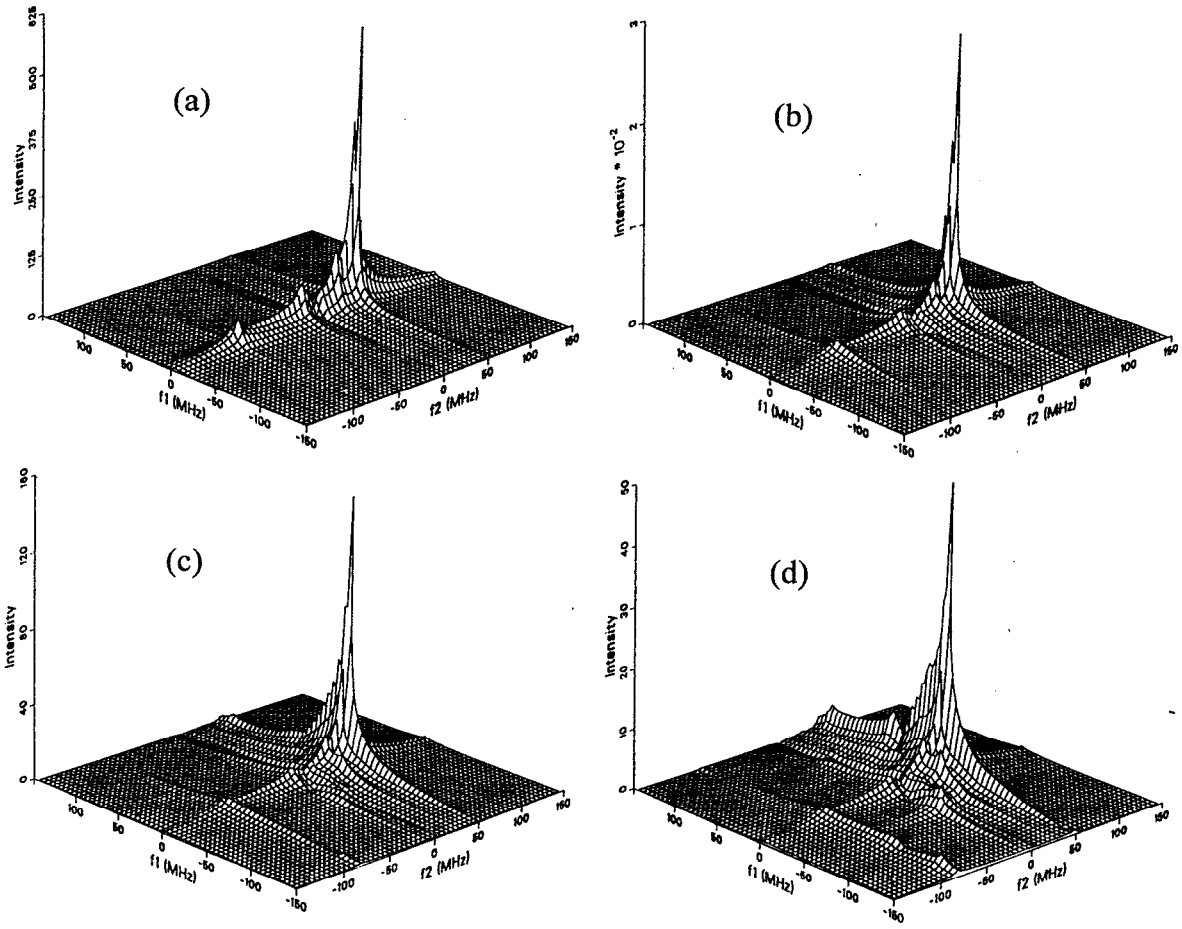

FIG. 13. 2D-echo-ELDOR spectra of the ^{15}N nitroxide ($I=1/2$) near the rigid limit ($R=10^5$ s^{-1}) for mixing times of (a) $T=0$ μs, i.e., the SECSY spectrum, (b) $T=0.5$ μs, (c) $T=2$ μs, (d) $T=5$ μs. The simulation parameters are: $R=10^5$ s^{-1}, $g_{xx}, g_{yy}, g_{zz}=2.0096, 2.0063, 2.0022$, $A_{xx}, A_{yy}, A_{zz}=9.12, 6.31, 46.84$ G, $\Delta_G=0.1$ G, $L^e_{\max}=30$, $L^o_{\max}=15$, $K_{\max}=14$, and $B_0=3200$ G. Pruned basis set was obtained with a 1% tolerance. Initial $t_1, t_2=0$ ns, steps in t_1 and t_2 (i.e., Δt_1 and Δt_2) are 3 ns, and 128 t_1, t_2 values are used for the 2D simulation.

inhomogeneous broadening in several motional regimes. We also described a method of obtaining homogeneous linewidths across the spectrum from the S_{c-} COSY signal.

The theory was applied to the case of rotational motion in complex fluids such as liquid crystals and membrane vesicles. The MOMD model was used to simulate experimental 2D-ESR spectra in such complex fluids.

Autopeaks of the 2D-ELDOR spectra near the rigid limit broaden as the mixing time increases, due to the development of motional crosspeaks. A method of obtaining the rotational correlation time from the rate of line broadening is described and related to recent experimental results.

The effect of motion and of an orienting potential on the nuclear modulation pattern was also demonstrated. A difference between the field-swept 2D-ESE and the absolute value SECSY spectrum was described in terms of a mixed phase problem, and the importance of obtaining a pure absorption spectrum was emphasized.

Finally, we wish to make a few comments about the range of applicability of the theory. It may be thought that the assumption of a simple Markov process to describe the rotational motion in fluids could be a limitation on the applicability of the stochastic Liouville equation. Actually, the SLE can be derived under very general conditions from the many-body Liouville equation using a few statistical assumptions for the rotating (and translating) molecule including spin.[11,42–44] It is quite possible that future 2D-FT ESR experiments will provide sufficient detail on molecular motions that a simple Markov process expressed by the Smoluchowski equation (of Appendix B) is no longer adequate, especially for very slow motions. In fact, as we pointed out some time ago,[45] augmented models of the motional dynamics are very likely required to fit ESR spectra. Fortunately, the assumption of a Markov process is not in itself particularly limiting, since one is able to write the SLE for a more complex Markov process in which all the slow variables which are relevant to the motional dynamics of the spin-bearing molecule are explicitly included in the form of a multidimensional Fokker–Planck equation.[11,42–44]

Procedures for constructing more sophisticated many-body Fokker–Planck equations to deal with rotational motions in liquids have been extensively reviewed by us.[46] For

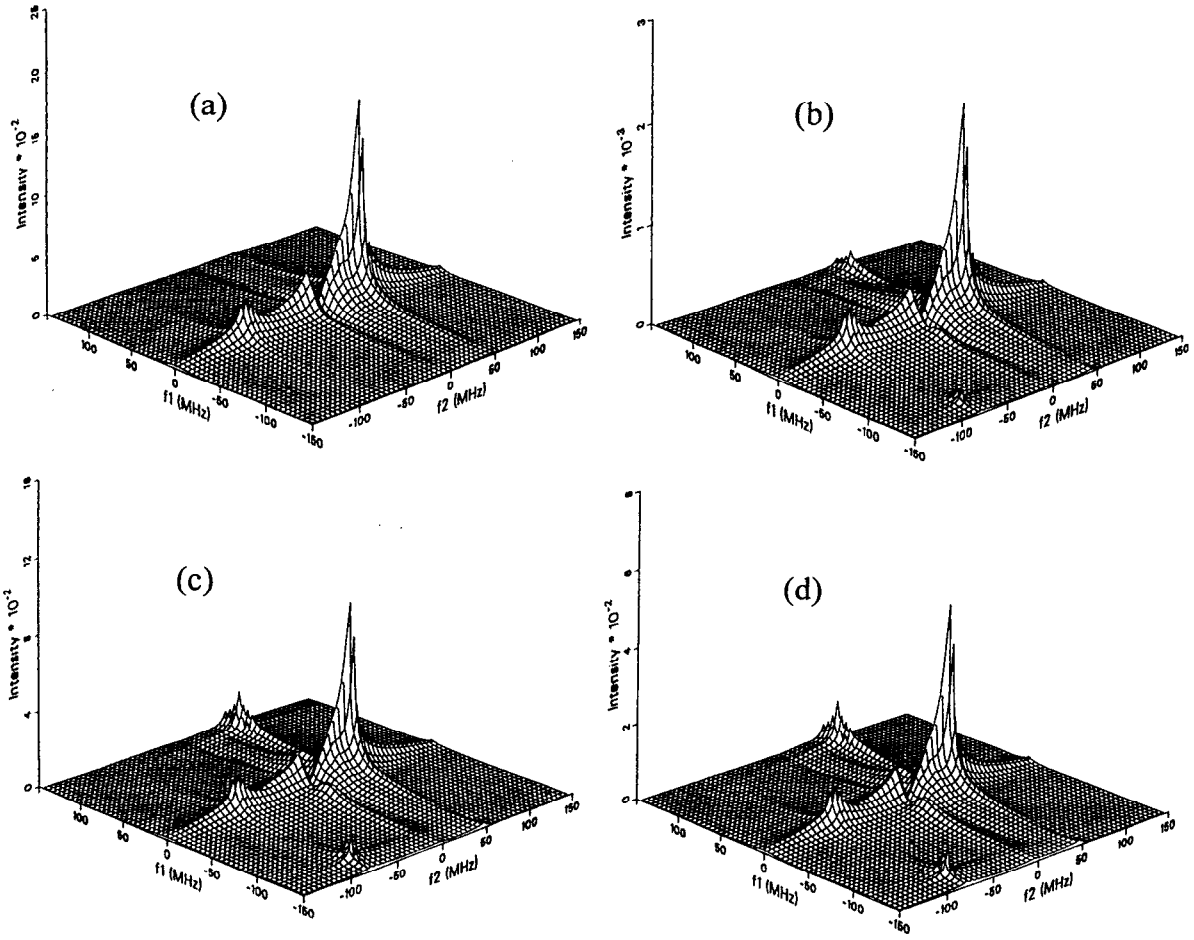

FIG. 14. 2D-echo-ELDOR spectra of the ^{15}N nitroxide ($I=1/2$) for restricted but fast motion based on the MOMD model averaged over 20 director tilt angles. (a) $T=0$ ns, i.e., the SECSY spectrum, (b) $T=100$ ns, (c) $T=500$ ns, (d) $T=1000$ ns. The simulation parameters are the same as in Fig. 13 except $R=10^7$ s^{-1}, $c_0^2=10.0$, $\Delta_G=0.1$ G, $L^e_{\max}=12$, $L^o_{\max}=9$, $K_{\max}=4$, and $B_0=3200$ G. Pruned basis set was obtained with a 2% tolerance. Initial $t_1,t_2=0$ ns, step size Δt_1, $\Delta t_2=3$ ns, and 128 t_1,t_2 values are used for the 2D simulation.

example, a model of particular relevance for slow-motional ESR studies is one of a loose "cage" of solvent molecules around the reorienting probe molecule, which is itself relaxing in the same time range as the probe molecule. (This may be regarded as a generalization of the MOMD model). The construction of such a "slowly relaxing local structure model" (SRLS), as well as other related models in the Fokker–Planck formalism is described elsewhere[43,47,48] and applied to highly viscous fluids.[48] The associated multidimensional Fokker–Planck operators, since they are Markovian, can then replace the simple Smoluchowski equation used in this work [as the $\Gamma(\Omega)$ in Eq. (1)] to provide a more detailed theory with which to analyze both cw and 2D-FT ESR spectra. In particular, we plan to report in the near future on the use of the SRLS model[46,48] for describing ESR spectra from viscous fluids by means of the SLE.[49] This analysis shows that better agreement between simulations and experimental data can be obtained when slow solvent modes are relevant, but the principal features of the spectra are usually not substantially affected by the use of such a more sophisticated model.

ACKNOWLEDGMENTS

This work was supported by NSF Grants Nos. CHE9313167 and DMR9210638 and NIH Grants Nos. GM25862 and RR07126. Computations were performed at the Cornell Theory Center. We thank David Schneider for many useful discussions during the course of this work.

APPENDIX A: MATRIX REPRESENTATION OF THE STOCHASTIC LIOUVILLE OPERATOR—THE SPIN HAMILTONIAN SUPEROPERATOR

The spin Hamiltonian in Liouville space can be expanded in terms of spherical tensor operators as

$$H=\sum_{\mu,l,m} F^{(l,m)*}_{\mu,L} A^{(l,m)}_{\mu,L}, \tag{A1}$$

where μ specifies the kind of interaction (Zeeman or hyperfine) and the $A^{(l,m)}_{\mu,L}$ are the irreducible tensor components of the spin operators in the laboratory frame. Since F is defined in the molecular frame, we need several transformations of

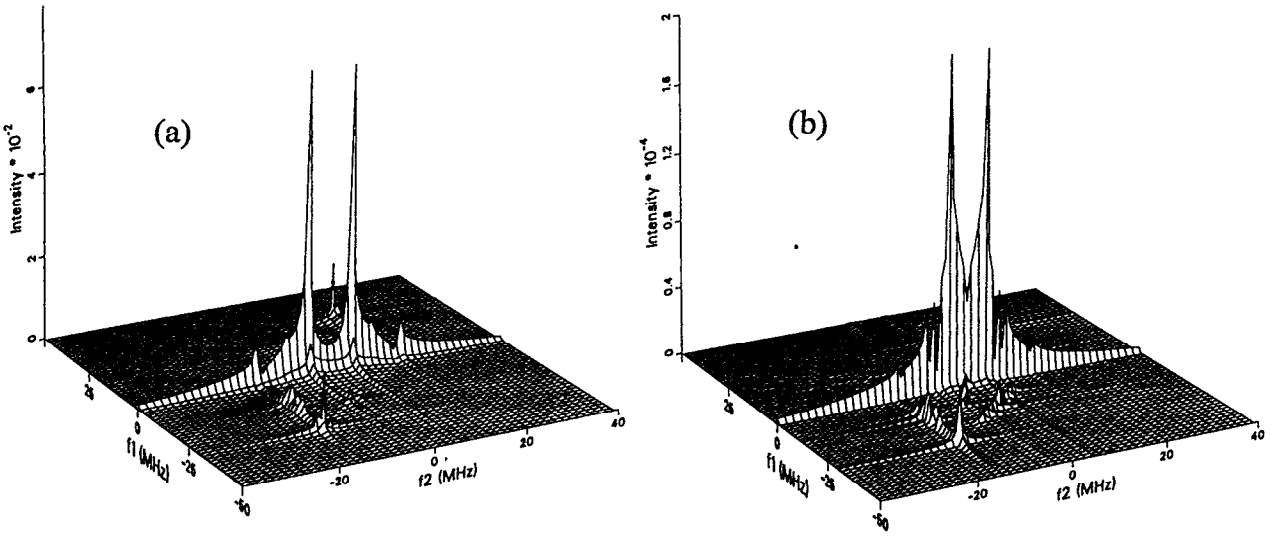

FIG. 15. SECSY spectra with nuclear modulation from the proton spin ($I=1/2$), for (a) $R=4.63\times10^3$ s^{-1}, no potential, $L_{\max}=92$, (b) MOMD spectrum averaged over 20 director tilt angles at $R=4.63\times10^7$ s^{-1}, $c_0^2=10.0$, $L_{\max}=30$. The parameters used for the simulation are: $g_{xx}=g_{yy}=g_{zz}=2.002$, $A_{xx}=A_{yy}=-3.25$ G, $A_{zz}=6.5$ G, $g_n=5.5854$ and $B_0=3200$ G. No extra inhomogeneous broadening is added in order to show the fine details of the modulation pattern.

axes from the lab frame to the molecular frame, which are represented by the Wigner rotation matrices. We will follow the transformation scheme defined in the references.[9,16] The relevant frames of reference in the order of transformations are: laboratory frame (L), director frame (d), diffusion frame (D), g-tensor frame (g), and hyperfine tensor frame (a). The director frame is included to describe uniaxial liquid crystals, whose director axis may be tilted away from the magnetic field axis by the "director tilt" angle ψ.

The g tensor in irreducible tensor form is[9]

$$
\begin{aligned}
&F_{g,g}^{(0,0)}=-\frac{1}{\sqrt{3}}\left(\frac{\beta_e}{\hbar}\right)(g_{xx}+g_{yy}+g_{zz}),\\
&A_{g,L}^{(0,0)}=-\frac{1}{\sqrt{3}}B_0S_z,\\
&F_{g,g}^{(2,0)}=\sqrt{\frac{2}{3}}\left(\frac{\beta_e}{\hbar}\right)\left[g_{zz}-\frac{1}{2}(g_{xx}+g_{yy})\right],\\
&A_{g,L}^{(2,0)}=\sqrt{\frac{2}{3}}B_0S_z\\
&F_{g,g}^{(2,\pm1)}=0,\quad A_{g,L}^{(2,\pm1)}=\mp\tfrac{1}{2}B_0S_\pm,\\
&F_{g,g}^{(2,\pm2)}=\frac{1}{2}\left(\frac{\beta_e}{\hbar}\right)(g_{xx}-g_{yy}),\quad A_{g,L}^{(2,\pm2)}=0.
\end{aligned}
\tag{A2}
$$

The corresponding components of the hyperfine tensor are

$$
\begin{aligned}
&F_{a,a}^{(0,0)}=-\frac{1}{\sqrt{3}}\left(\frac{g_e\beta_e}{\hbar}\right)(A_{xx}+A_{yy}+A_{zz}),\\
&A_{a,L}^{(0,0)}=-\frac{1}{\sqrt{3}}\left[S_zI_z+\frac{1}{2}(S_+I_-+S_-I_+)\right],
\end{aligned}
$$

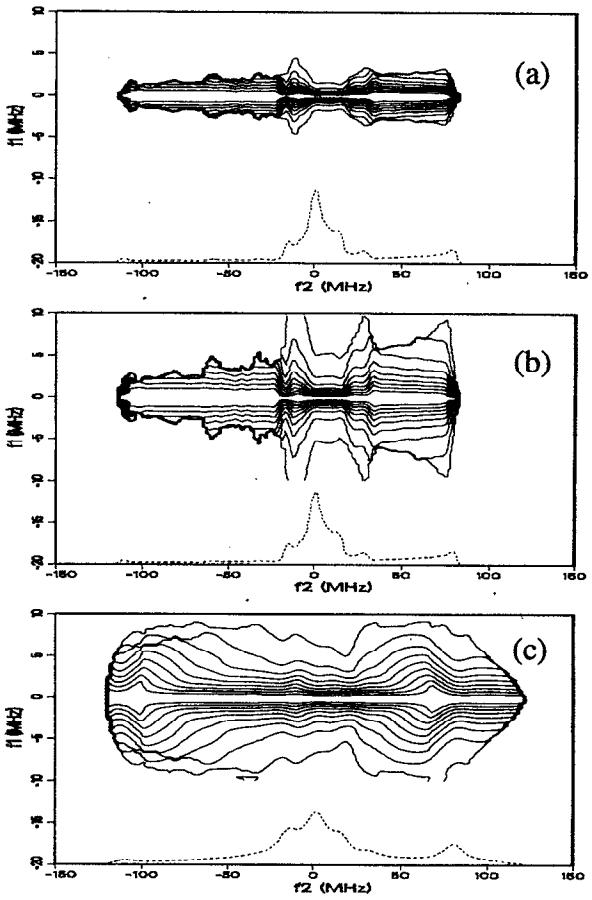

FIG. 16. Normalized contour plots near the rigid limit. (a) Pure absorption spectrum (easily obtained in the field-swept ESE experiment); (b) pure absorption along the f_2 axis, and absolute-value plot along the f_1 axis; (c) absolute-value plot along both axes (e.g., a SECSY spectrum using a simple 2D-fast Fourier transform without phase correction). The parameters for the simulation are the same as in Fig. 9.

$$F_{a,a}^{(2,0)}=\sqrt{\frac{2}{3}}\left(\frac{g_e\beta_e}{\hbar}\right)\left[A_{zz}-\frac{1}{2}(A_{xx}+A_{yy})\right],$$

$$A_{a,L}^{(2,0)}=\sqrt{\frac{2}{3}}\left[S_zI_z-\frac{1}{4}(S_+I_-+S_-I_+)\right],$$

$$F_{a,a}^{(2,\pm1)}=0,\quad A_{a,L}^{(2,\pm1)}=\mp\frac{1}{2}(S_\pm I_z+S_zI_\pm), \tag{A3}$$

$$F_{a,a}^{(2,\pm2)}=\frac{1}{2}\left(\frac{g_e\beta_e}{\hbar}\right)(A_{xx}-A_{yy}),\quad A_{a,L}^{(2,\pm2)}=\frac{1}{2}S_\pm I_\pm .$$

The nuclear Zeeman term retaining only the isotropic contribution may be written as

$$F_{n,n}^{(0,0)}=-\frac{g_n\beta_n}{\hbar},\quad A_{n,L}^{(0,0)}=-B_0I_z. \tag{A4}$$

After explicitly including the transformations of the frames of reference, the Hamiltonian in Eq. (A1) can be rewritten as

$$H=\sum_{\substack{\mu,l,m\\ m',m''}} d^l_{mm'}(\psi)\mathscr{D}^{\,l}_{m'm''}(\Omega)F_{\mu,D}^{(l,m'')*}A_{\mu,L}^{(l,m)}, \tag{A5}$$

where Ω defines the Euler angles that transform the director (d) frame to the diffusion (D) frame and the $d^l_{mm'}$ are the reduced Wigner rotation matrix elements. The spherical tensor components, $F_{\mu,D}^{(l,m)}$ can be written in terms of the principal values of the corresponding tensor μ as follows:

$$F_{g,D}^{(l,m)*}=\sum_{m'}\mathscr{D}^{\,l}_{mm'}(\Omega_{D\to g})F_{g,g}^{(l,m')*},$$

$$F_{a,D}^{(l,m)*}=\sum_{m'}\mathscr{D}^{\,l}_{mm'}(\Omega_{D\to a})F_{a,a}^{(l,m')*} \tag{A6}$$

$$=\sum_{m',m''}\mathscr{D}^{\,l}_{mm'}(\Omega_{D\to g})\mathscr{D}^{\,l}_{m'm''}(\Omega_{g\to a})F_{a,a}^{(l,m')*}.$$

The "diffusion tilt angle" $\Omega_{D\to g}=(\alpha_D,\beta_D,\gamma_D)$ defines the transformation from the diffusion frame to the principal axes of the g-tensor frame.

Then the matrix representation of the Hamiltonian superoperator in the basis set of the Liouville space defined in Eq. (6) can be shown to be

$$\langle p_1^S,q_1^S,p_1^I,q_1^I;L_1,M_1,K_1|\mathscr{H}^\times|p_2^S,q_2^S,p_2^I,q_2^I;L_2,M_2,K_2\rangle$$

$$=N_L(L_1,L_2)(-1)^{M_1+K_1}\sum_{\mu,l}\langle p_1^S,q_1^S,p_1^I,q_1^I|A_{\mu,L}^{(l,\Delta p)^\times}|p_2^S,q_2^S,p_2^I,q_2^I\rangle d^l_{\Delta p,M_1-M_2}(\psi)F_{\mu,D}^{(l,K_1-K_2)*}$$

$$\times\begin{pmatrix}L_1 & l & L_2\\ M_1 & M_2-M_1 & -M_2\end{pmatrix}\begin{pmatrix}L_1 & l & L_2\\ K_1 & K_2-K_1 & -K_2\end{pmatrix}, \tag{A7}$$

where $N_L(L_1,L_2)=(2L_1+1)^{1/2}(2L_2+1)^{1/2}$ and $\Delta p=p_1^S-p_2^S+p_1^I-p_2^I$.

The matrix representation of $A_{a,L}^{(l,m)^\times}$ can be derived from Eqs. (A2)–(A4)[16]

$$\langle p_1^S,q_1^S,p_1^I,q_1^I|A_{a,L}^{(l,m)^\times}|p_2^S,q_2^S,p_2^I,q_2^I\rangle$$

$$=\delta_{m,\Delta p}\delta_{|\Delta p^S|,|\Delta q^S|}\delta_{|\Delta p^I|,|\Delta q^I|}\delta_{\Delta p^S\Delta p^I,\Delta q^S\Delta q^I}(-1)^{\Delta p}(2l+1)^{1/2}\begin{pmatrix}1 & 1 & l\\ \Delta p^S & \Delta p^I & -\Delta p\end{pmatrix}S_A, \tag{A8}$$

where $\Delta p^S=p_1^S-p_2^S$, $\Delta q^S=q_1^S-q_2^S$, $\Delta p^I=p_1^I-p_2^I$, and $\Delta q^I=q_1^I-q_2^I$. The quantity S_A is defined as follows:

$$S_A=\begin{cases}(p_1^Sq_1^I+p_1^Iq_1^S)/2 & \text{if}\quad \Delta p^S=0,\quad \Delta p^I=0\\ -(p_1^S\Delta p^I+q_1^S\Delta q^I)K_I/\sqrt{8} & \text{if}\quad \Delta p^S=0,\quad \Delta p^I\neq0\\ -(p_1^I\Delta p^S+q_1^I\Delta q^S)/\sqrt{8} & \text{if}\quad \Delta p^S\neq0,\quad \Delta p^I=0\\ \Delta p^S\Delta q^IK_I/2 & \text{if}\quad \Delta p^S\neq0,\quad \Delta p^I\neq0\end{cases}, \tag{A9}$$

where

$$K_I=[I(I+1)-(q_1^I\Delta q^I+p_1^I\Delta p^I)(q_1^I\Delta q^I+p_1^I\Delta p^I-2)/4]^{1/2}.$$

The matrix elements of $A_{g,L}^{(l,m)^\times}$ and $A_{n,L}^{(l,m)^\times}$ can be written similarly as

$$\langle p_1^S,q_1^S,p_1^I,q_1^I|A_{g,L}^{(l,m)^\times}|p_2^S,q_2^S,p_2^I,q_2^I\rangle$$

$$=\delta_{m,\Delta p}\delta_{|\Delta p|,|\Delta q|}\delta_{\Delta p^I,0}\delta_{\Delta q^I,0}B_0(-1)^{\Delta p}(2l+1)^{1/2}$$

$$\times\begin{pmatrix}1 & 1 & l\\ \Delta p & 0 & -\Delta p\end{pmatrix}(p_1^S\delta_{\Delta p^S,0}-\Delta q^S(1-\delta_{\Delta p^S,0})/\sqrt{2}),$$

$$\langle p_1^S, q_1^S, p_1^I, q_1^I | A_{n,L}^{(l,m)\times} | p_1^S, q_1^S, p_2^I, q_2^I \rangle = -\delta_{m,0}\delta_{\Delta p^S,0}\delta_{\Delta q^S,0}\delta_{\Delta p^I,0}\delta_{\Delta q^I,0}B_0 p_1^I . \quad \text{(A10)}$$

Equations (A6)–(A10) describe the spin Hamiltonian superoperator in detail.

APPENDIX B: MATRIX REPRESENTATION OF THE STOCHASTIC LIOUVILLE OPERATOR—THE RELAXATION SUPEROPERATOR AND THE STARTING VECTOR

The relaxation superoperator $\Gamma(\Omega)$ includes all the sources of relaxation of the system. The relaxation mechanisms of interest in ESR are well described elsewhere,[50] and we will give a brief summary here just for completeness.

The overall $\Gamma(\Omega)$ operator is taken as a superposition of the terms

$$\Gamma(\Omega)=\Gamma_{\rm iso}+\Gamma_U+\Gamma_{\rm dj}+\Gamma_{\rm ex}+\Gamma_{W_e}+\Gamma_{W_n}, \quad \text{(B1)}$$

where $\Gamma_{\rm iso}$ represents rotational diffusion in isotropic fluids, Γ_U is the rotational diffusion correction for liquid crystals, $\Gamma_{\rm dj}$ is the discrete jump model among equivalent sites, $\Gamma_{\rm ex}$ represents Heisenberg spin exchange, and Γ_{W_e} and Γ_{W_n} account for rotationally independent electronic and nuclear spin flip rates, respectively.

Rotational diffusion in isotropic fluids assuming the diffusional motion is axially symmetric was shown to be[16]

$$\langle L_1, M_1, K_1, j_1^K, j_1^M | \Gamma_{\rm iso} | L_2, M_2, K_2, j_2^K, j_2^M \rangle_{KM} = \delta_{j_1^M, j_2^M}\delta_{j_1^K, j_2^K}\delta_{L_1,L_2}\delta_{M_1,M_2}\delta_{K_1,K_2}\{R_\perp L_1(L_1+1) \times [1+\tau_\perp R_\perp L_1(L_1+1)]^{-E_\perp} + K_1^2[R_\parallel(1+\tau_\parallel R_\parallel K_1^2)^{-E_\parallel} - R_\perp(1+\tau_\perp' R_\perp K_1^2)^{-E_\perp'}]\}. \quad \text{(B2)}$$

The possible limiting situations are (i) Brownian motion: $\tau=0$, $E=0$; (ii) free diffusion: $\tau\neq 0$, $E=1/2$; and (iii) jump diffusion: $\tau\neq 0$, $E=1$.[50] The expression for $\Gamma_{\rm iso}$ was recently generalized to the nonaxial case for Brownian diffusion:[15]

$$\langle L_1, M_1, K_1, j_1^K, j_1^M | \Gamma_{\rm iso} | L_2, M_2, K_2, j_2^K, j_2^M \rangle_{KM} = \delta_{j_1^M, j_2^M}\delta_{j_1^K, j_2^K}\delta_{L_1,L_2}\delta_{M_1,M_2}\left[\delta_{K_1,K_2}\left(\frac{R_x+R_y}{2}[L_1(L_1+1)-K_1^2]+R_z K_1^2\right) + (\delta_{K_1-2,K_2}N_+(L_1,K_1-2)+\delta_{K_1+2,K_2}N_-(L_1,K_1+2))N_K(K_1,K_2)^{-1}\frac{(R_x-R_y)}{4}\right], \quad \text{(B3)}$$

where $N_\pm(L,K)=[(L\mp K-1)(L\mp K)(L\pm K+1)(L\pm K+2)]^{1/2}$.

The diffusion operator in the presence of an anisotropic orienting potential is formulated in terms of the symmetrized Smoluchowski equation.[15,16,51] The orienting potential is assumed to be uniaxial and expanded in terms of spherical harmonics, i.e.,

$$U(\Omega)=-k_B T{\sum_{L,K}}' \epsilon_K^L \mathscr{D}_{0K}^L(\Omega), \quad \text{(B4)}$$

where the prime indicates that the summation is restricted to even values of L and K up to 4 for convenience, and the expansion coefficients have the property that

$$\epsilon_K^L=\epsilon_{-K}^L=\epsilon_K^{L*}. \quad \text{(B5)}$$

Then Γ_U, which is the correction term due to the potential can be written as $\Gamma_U=\Sigma_{L,K}X_K^L\mathscr{D}_{0K}^L$, where the coefficients X_K^L are

$$X_K^L=-\frac{1}{2}\left((\epsilon_{K+2}^L N_-(L,K+2)+\epsilon_{K-2}^L N_+(L,K-2))\frac{R_x-R_y}{4}+\epsilon_K^L[L(L+1)-K^2]\frac{R_x+R_y}{2}+\epsilon_K^L K^2 R_z\right) - \frac{2L+1}{4}\sum_{L_1,K_1,L_2,K_2}\epsilon_{K_1}^{L_1}\epsilon_{K_2}^{L_2}\begin{pmatrix}L_1 & L & L_2\\ 0 & 0 & 0\end{pmatrix}\left[\frac{R_x-R_y}{4}\left[M_+(L_1,K_1)M_+(L_2,K_2)\begin{pmatrix}L_1 & L & L_2\\ K_1+1 & -K & K_2+1\end{pmatrix} + M_-(L_1,K_1)M_-(L_2,K_2)\begin{pmatrix}L_1 & L & L_2\\ K_1-1 & -K & K_2-1\end{pmatrix}\right] + \frac{R_x+R_y}{2}M_+(L_1,K_1)M_-(L_2,K_2)\begin{pmatrix}L_1 & L & L_2\\ K_1+1 & -K & K_2-1\end{pmatrix} + R_z K_1 K_2\begin{pmatrix}L_1 & L & L_2\\ K_1 & -K & K_2\end{pmatrix}\right]. \quad \text{(B6)}$$

The corresponding matrix elements in the M-symmetrized basis are[15]

$$\langle L_1,M_1,K_1,j_1^K,j_1^M|\Gamma_U|L_2,M_2,K_2,j_2^K,j_2^M\rangle_{KM}$$

$$=\delta_{M_1,M_2}\delta_{j_1^M,j_2^M}\delta_{j_1^K,j_2^K}N_L(L_1,L_2)N_K(K_1,K_2)(-1)^{M_1+K_1}\sum_L\begin{pmatrix}L_1 & L & L_2\\ M_1 & 0 & -M_1\end{pmatrix}\left[X^L_{K_1-K_2}\begin{pmatrix}L_1 & L & L_2\\ K_1 & K_2-K_1 & -K_2\end{pmatrix}\right.$$

$$\left.+j_2^K(-1)^{L_2+K_2}X^L_{K_1+K_2}\begin{pmatrix}L_1 & L & L_2\\ K_1 & -K_1-K_2 & K_2\end{pmatrix}\right]. \tag{B7}$$

The model of discrete jump amongst equivalent sites in the particular case that these sites are connected by a rotation around the diffusional z axis can be written as

$$\langle L_1,M_1,K_1,j_1^K,j_1^M|\Gamma_{\rm dj}|L_2,M_2,K_2,j_2^K,j_2^M\rangle_{KM}=\delta_{L_1,L_2}\delta_{M_1,M_2}\delta_{K_1,K_2}\delta_{j_1^M,j_2^M}\delta_{j_1^K,j_2^K}\frac{1-\delta^{n_s}_{K_1}}{\tau_{\rm dj}}, \tag{B8}$$

where $\tau_{\rm dj}$ is the mean time between jumps, n_s is the number of equivalent sites and the only nonzero δ^n_K is 1 if K is a multiple of n.

The Heisenberg spin exchange operator $\Gamma_{\rm ex}$ has been re-derived for the model in which spins exchange between molecules of arbitrary orientation.[52] It can yield complete exchange narrowing even for slow-motional spectra. The matrix elements can be written as

$$\langle p_1^S,q_1^S,p_1^I,q_1^I;L_1,M_1,K_1,j_1^K,j_1^M|\Gamma_{\rm ex}|p_2^S,q_2^S,p_2^I,q_2^I;L_2,M_2,K_2,j_2^K,j_2^M\rangle_{KM}$$

$$=\omega_{HE}\delta_{j_1^M,j_2^M}\delta_{j_1^K,j_2^K}\delta_{L_1,L_2}\delta_{K_1,K_2}\delta_{p_1^S,p_2^S}\left(\delta_{q_1^I,q_2^I}-\frac{1}{2I+1}\,\delta_{p_1^I,0}\delta_{L_1,0}\right)$$

$$\times\left[\delta_{p_1^S,0}\,\frac{1}{2}\,(\delta_{M_1,M_2}\delta_{p_1^I,p_2^I}+j_2^M(-1)^{L_2+M_2}\delta_{M_1,-M_2}\delta_{p_1^I,-p_2^I})+\delta_{|p_1^S|,1}\delta_{M_1,M_2}\delta_{p_1^I,p_2^I}\right], \tag{B9}$$

where ω_{HE} is the effective spin exchange frequency.

The rotationally independent electron spin flip rate W_e is included as follows:

$$\langle 0,1,p_1^I,q_1^I;L_1,M_1,j_1^K,j_1^M|\Gamma_{W_e}|0,1,p_2^I,q_2^I;L_2,M_2,j_2^K,j_2^M\rangle_{KM}$$

$$=W_e\delta_{j_1^M,j_2^M}\delta_{j_1^K,j_2^K}\delta_{L_1,L_2}\delta_{K_1,K_2}\delta_{|M_1|,|M_2|}\delta_{|p_1^I|,|p_2^I|}\delta_{q_1^I,q_2^I}(\delta_{p_1^I,p_2^I}\delta_{M_1,M_2}+j_2^M(-1)^{L_2+M_2}\delta_{p_1^I,-p_2^I}\delta_{M_1,-M_2}). \tag{B10}$$

The rotationally independent nuclear spin flip rate W_n is also included to account for the additional nuclear spin–flip rates other than from the rotational motion[11,18,19,53]

$$\langle 0,1,p_1^I,q_1^I;L_1,M_1,j_1^K,j_1^M|\Gamma_{W_n}|0,1,p_2^I,q_2^I;L_2M_2,j_2^K,j_2^M\rangle_{KM}$$

$$=W_n\delta_{j_1^M,j_2^M}\delta_{j_1^K,j_2^K}\delta_{L_1,L_2}\delta_{K_1,K_2}\delta_{M_1,M_2}\delta_{\Delta p^I,0}[\delta_{p_1^I,0}(\delta_{\Delta q^I,0}-\delta_{\Delta q^I,2})+\tfrac{7}{6}\delta_{|p_1^I|,1}] \tag{B11}$$

for $I=1/2$ and

$$\langle 0,1,p_1^I,q_1^I;L_1,M_1,j_1^K,j_1^M|\Gamma_{W_n}|0,1,p_2^I,q_2^I;L_2,M_2,j_2^K,j_2^M\rangle_{KM}$$

$$=W_n\delta_{j_1^M,j_2^M}\delta_{j_1^K,j_2^K}\delta_{L_1,L_2}\delta_{K_1,K_2}\delta_{M_1,M_2}\delta_{\Delta p^I,0}[\delta_{p_1^I,0}(\delta_{\Delta q^I,0}(2-\delta_{|q_1^I|,2I})-\delta_{\Delta q^I,2})+\delta_{p_1^I,1}(\tfrac{13}{6}\delta_{\Delta q^I,0}-\delta_{\Delta q^I,2})+\tfrac{11}{3}\delta_{|p_1^I|,2}\delta_{\Delta q^I,0}] \tag{B12}$$

for $I=1$.

The starting vector elements in the M-symmetrized basis set are

$${}_{KM}\langle p^S,q^S,p^I,q^I;L,M,K,j^K,j^M|v_\pm\rangle$$

$$=\delta_{p^S,\pm1}\delta_{p^I,0}\delta_{M,0}\delta_{j^K,1}\delta_{j^M,1}(2I+1)^{-1/2}\left(\frac{2}{(1+\delta_{K,0})}\right)^{1/2}\left(\frac{2L+1}{8\pi^2}\right)^{1/2}\int d\Omega\; P(\Omega)^{1/2}\,{\rm Re}\{\mathscr{D}^L_{0K}\}. \tag{B13}$$

This completes the matrix representation of the stochastic Liouville operator in the M-symmetrized basis.

[1] J. Gorcester and J. Freed, J. Chem. Phys. **85**, 5375 (1986).
[2] J. Gorcester and J. H. Freed, J. Chem. Phys. **88**, 4678 (1988).
[3] J. Gorcester, S. B. Rananavare, and J. H. Freed, J. Chem. Phys. **90**, 5764 (1989).
[4] B. R. Patyal, R. H. Crepeau, D. Gamliel, and J. H. Freed, Chem. Phys. Lett. **175**, 445 (1990).
[5] B. R. Patyal, R. H. Crepeau, D. Gamliel, and J. H. Freed, Chem. Phys. Lett. **175**, 453 (1990).
[6] S. Lee, B. R. Patyal, S. Saxena, R. H. Crepeau, and J. H. Freed, Chem. Phys. Lett. **211**, 397 (1994).
[7] R. H. Crepeau, S. Saxena, S. Lee, B. R. Patyal, and J. H. Freed, Biophys. J. **66**, 1489 (1994).
[8] J. H. Freed, G. V. Bruno, and C. F. Polnaszek, J. Phys. Chem. **75**, 3385 (1971).
[9] D. J. Schneider and J. H. Freed, in *Spin Labeling: Theory and Application*, edited by L. J. Berliner and J. Reuben (Plenum, New York, 1989).
[10] G. Moro and J. H. Freed, J. Chem. Phys. **74**, 3757 (1981).
[11] D. J. Schneider and J. H. Freed, Adv. Chem. Phys. **73**, 387 (1989).
[12] K. V. Vasavada, D. J. Schneider, and J. H. Freed, J. Chem. Phys. **86**, 647 (1987).
[13] R. H. Crepeau, S. B. Rananavare, and J. H. Freed, in *10th International EPR Symposium* (Rocky Mountain Conference, Denver, 1987).
[14] D. E. Budil, S. Lee, and J. H. Freed (to be published).
[15] K. A. Earle, D. E. Budil, and J. H. Freed, J. Phys. Chem. **97**, 13289 (1993).
[16] E. Meirovitch, D. Igner, E. Igner, G. Moro, and J. H. Freed, J. Chem. Phys. **77**, 3915 (1982).
[17] L. J. Schwartz, A. E. Stillman, and J. H. Freed, J. Chem. Phys. **77**, 5410 (1982).
[18] L. J. Schwartz, Ph.D. thesis, Cornell University, 1984.
[19] L. Schwartz, G. L. Millhauser, and J. H. Freed, Chem. Phys. Lett. **127**, 60 (1986).
[20] G. L. Millhauser and J. H. Freed, J. Chem. Phys. **81**, 37 (1984).
[21] In the actual experiments one is able to correct the signal for nonuniform coverage (Ref. 7). The computational complexities introduced by considering microwave pulses of finite amplitude is a matter we plan to discuss elsewhere.
[22] L. J. Schwartz, E. Meirovitch, J. A. Ripmeester, and J. H. Freed, J. Phys. Chem. **87**, 4453 (1983).
[23] R. R. Ernst, G. Bodenhausen, and A. Wokaun, *Principles of Nuclear Magnetic Resonance in One and Two Dimensions* (Oxford, New York, 1987).
[24] J. H. Freed, J. Chem. Phys. **41**, 2077 (1964).
[25] D. Gamliel and J. H. Freed, J. Magn. Reson. **89**, 60 (1990).
[26] R. N. Zare, *Angular Momentum* (Wiley, New York, 1988).
[27] G. H. Golub and C. F. V. Loan, *Matrix Computations* (The Johns Hopkins University Press, Baltimore, 1989).
[28] J. K. Cullum and R. A. Willoughby, *Lanczos Algorithms for Large Symmetric Eigenvalue Computations* (Birkhauser, Boston, 1985).
[29] W. H. Press, S. A. Teukolsky, W. T. Vetterling, and B. P. Flannery, *Numerical Recipes* (Cambridge University, New York, 1992).
[30] It seems reasonable to expect that Eq. (32) can be the basis of a reliable test for spurious eigenvalues. A good eigenvalue will yield an $\mathbf{x}'$ that is asymptotically independent of s as $s \rightarrow 0$.
[31] R. G. Gordon and T. Messenger, in *Electron Spin Relaxation in Liquids*, edited by L. T. Muus and P. W. Atkins (Plenum, New York, 1972).
[32] G. V. Bruno, Ph.D. thesis, Cornell University, 1973.
[33] S. Lee, B. R. Patyal, and J. H. Freed, J. Chem. Phys. **98**, 3665 (1993).
[34] E. Meirovitch and J. H. Freed, J. Phys. Chem. **88**, 4995 (1984).
[35] M. Ge and J. H. Freed, Biophys. J. **65**, 2106 (1993).
[36] J. H. Freed, J. Phys. Chem. **78**, 1155 (1974).
[37] J. H. Freed, in *Time Domain Electron-Spin Resonance*, edited by L. Kevan and R. N. Schwartz (Wiley, New York, 1979).
[38] J. Gorcester, G. L. Millhauser, and J. H. Freed, in *Advanced EPR: Applications in Biology and Biochemistry*, edited by A. J. Hoff (Elsevier, Amsterdam, 1989).
[39] G. L. Millhauser and J. H. Freed, J. Chem. Phys. **85**, 63 (1986).
[40] J. Gorcester and J. H. Freed, J. Magn. Reson. **78**, 292 (1988).
[41] J. Gorcester, G. L. Millhauser, and J. H. Freed, in *Modern Pulsed and Continuous Wave Electron Spin Resonance*, edited by L. Kevan and M. K. Bowman (Wiley, New York, 1990).
[42] L. P. Hwang and J. H. Freed, J. Chem. Phys. **63**, 118 (1975).
[43] A. E. Stillman and J. H. Freed, J. Chem. Phys. **72**, 550 (1980).
[44] W. A. Wassam and J. H. Freed, J. Chem. Phys. **76**, 6150 (1982).
[45] J. S. Hwang, R. P. Mason, L. Hwang, and J. H. Freed, J. Phys. Chem. **79**, 489 (1975).
[46] A. Polimeno and J. H. Freed, Adv. Chem. Phys. **83**, 89 (1993).
[47] A. Polimeno and J. H. Freed, Chem. Phys. Lett. **174**, 338 (1990).
[48] A. Polimeno and J. H. Freed, Chem. Phys. Lett. **174**, 481 (1990).
[49] A. Polimeno and J. H. Freed (to be published).
[50] J. H. Freed, in *Spin Labeling: Theory and Application*, edited by L. J. Berliner (Academic, New York, 1976).
[51] C. F. Polnaszek and J. H. Freed, J. Phys. Chem. **79**, 2283 (1975).
[52] J. H. Freed (unpublished results).
[53] J. H. Freed, D. S. Leniart, and J. S. Hyde, J. Chem. Phys. **47**, 2762 (1967).